Distribution of Higher-Order Structures in Injection-Molded Polypropylenes

MITSUYOSHI FUJIYAMA* and TETSUO WAKINO

Polymer Development Laboratory, Tokuyama Soda Co., Ltd., Tokuyama-shi, Yamaguchi-ken 745, Japan

SYNOPSIS

Flexural test specimens were injection-molded from six homoisotactic polypropylenes with MFI = 0.49–25.1 dg/min under cylinder temperatures of 200–320°C. Distributions in the flow direction of higher-order structures such as crystallinity X_c, thickness of skin layer, a^*-axis-oriented component fraction $[A^*]$, and crystalline orientation functions and distributions in the thickness direction of higher-order structures such as X_c, β-crystal contents, $[A^*]$, and crystalline orientation functions were studied. These higher-order structures are inhomogeneous in the flow and thickness directions, which strongly influences the product properties such as mechanical and thermal properties. Molecular orientation process in injection molding was theoretically analyzed from a viewpoint of growth of recoverable shear strain at the gate and its relaxation in the cavity, which could considerably well explain the variations in the flow and thickness directions of the quantities such as thickness of the skin layer and crystalline orientation functions which express the degree of molecular orientation.

INTRODUCTION

In injection molding of thermoplastics, since molten resin solidifies under inhomogeneous stress and cooling conditions, the inner structures of the molded article are inhomogeneous, influencing the product properties. Consequently, it is important in injection molding technology of thermoplastics to clarify the influences of the primary structures of resin and molding conditions on the inhomogeneous structure of the molded article.

Many studies have so far been carried out on the distribution of higher-order structures in injection-molded thermoplastics. Table I summarizes previous studies on distribution of higher-order structures in injection-molded polypropylenes. The shapes of moldings studied are mainly simple shape test specimens. The influences of resin characteristics such as molecular weight, molecular weight distribution, glass fiber content, and talc content and molding conditions such as cavity thickness, cylinder temperature (resin temperature), mold temperature, injection speed, injection pressure, holding pressure, and cooling time are studied. Higher-order structures studied are crystalline texture (morphology), crystallinity, β-crystal content, crystal orientation state, degrees of crystalline and amorphous orientations, thickness of skin layer, glass fiber concentration, and orientation of talc. Directions studied are flow direction (MD) and thickness direction (ND).

In the present paper, we will report studies on the influences of molecular weight and cylinder temperature on distributions in the flow direction of higher-order structures such as crystallinity X_c, thickness of skin layer, a^*-axis-oriented component fraction $[A^*]$, and crystalline orientation functions and distributions in the thickness direction of higher-order structures such as X_c, β-crystal content, $[A^*]$, and crystalline orientation functions in injection-molded polypropylenes. In addition, a theoretical analysis of molecular orientation process will be presented.

EXPERIMENTAL

Samples

The resins used in this experiment were six homoisotactic polypropylens manufactured by Tokuyama

* To whom correspondence should be addressed.

Journal of Applied Polymer Science, Vol. 43, 57–81 (1991)
 CCC 0021-8995/91/010057-25$04.00

Table I Previous Studies on Distribution of Higher-Order Structures in Injection-Molded Polypropylenes

Author	Year	Shape of Molding	Influence of[a]	Higher-Order Structure[b]	Direction[c]	Ref.
Kantz et al.	1972	Tensile specimen	RT, IP	Crystalline texture	ND	1
Fitchmun and Mencik	1973	Rectangular plate	RT, MT, IS	Crystalline morphology	ND	2
Mencik and Fitchmun	1973	Rectangular plate	RT, IS	Crystal orientation state	ND	3
Menges et al.	1976	Rectangular plate	RT, MT	Crystalline texture, X_c	ND	4
Krsova	1977	Angle bar	RT	Thickness of skin layer	MD	5
Matsumoto et al.	1979	Bar	RT, MT, IP, IS, Ct	Crystalline texture	ND	6
Hirose et al.	1980	Rectangular plate		Δn, Thickness of skin layer	ND, MD	7
Trotignon et al.	1982	Tensile specimen	IS, IP	X_c, X-ray orientation degree, β-Crystal content	MD	8
Altendorfer and Geymayer	1983	Beaker	MW	Δn, Thickness of skin layer	MD	9
Altendorfer and Seitl	1984	Rectangular plate	MW, MWD, RT	Δn, Thickness of skin layer	MD	10
Altendorfer and Seitl	1986	Bar, Beaker	MW, MWD, RT	Thickness of skin layer	MD	11
Kamal et al.	1986	Rectangular plate	Glass fiber content	Fiber concentration, Crystalline and amorphous orientation degrees	MD, ND	12
Trotignon and Verdu	1987	Tensile specimen	MW, IS, HP	X_c, β-Crystal content, X-ray orientation degree, Crystalline and amorphous orientation degrees	ND, MD	13 14
Koppelmann et al.	1987	Rectangular plate	MWD, RT, MT, IS, HP	Δn, Thickness of skin layer	ND, MD	15
Fleischmann and Koppelmann	1987	Rectangular plate	MWD, RT, MT, IS, HP	Δn	MD, ND	16
Menges et al.	1987	Angle bar	RT, IS, HP	Δn, X_c, Thickness of skin layer	ND, MD	17
Kubota	1987	Rectangular plate	CT, MT, IP	Fluorescent orientation degree	MD, ND	18
Houska and Brummell	1987 1988	Square plate		X_c, Crystalline amorphous orientation degrees	ND	19 20
Murphy et al.	1988	Square plate	MW, RT	Crystalline texture, β-Crystal content, X_c, X-ray orientation degree	ND, MD	21 22
Fleischmann and Koppelmann	1988	Rectangular plate	MWD, RT, MT, IP, IS	Δn, Thickness of skin layer	ND, MD	23
Menges et al.	1988	Square plate	Cavity thickness, RT, IS	Degree of molecular orientation, X_c	MD	24
Fleischmann et al.	1989	Disc	HP	Orientation state of lamellae, X_c	MD, ND	25
Fleischmann	1989	Rectangular plate	MWD, RT, IS	Δn, Thickness of skin layer	MD, ND	26
Fujiyama and Wakino	1991	Bar	Talc content, CT	Orientation states of talc and PP crystal	ND	27

[a] MW = molecular weight; MWD = molecular weight distribution; RT = resin temperature; CT = cylinder temperature; MT = mold temperature; IS = injection speed; IP = injection pressure; HP = holding pressure; Ct = cooling time.
[b] X_c = crystallinity, Δn = birefringence.
[c] MD = machine direction; ND = normal direction.

Soda Co., Ltd. Table II shows characteristics of the samples. Melt flow index (MFI) was measured at 230°C under a load of 2160 g according to the ASTM D 1238-86T. Molecular weights were measured at 135°C with a gel permeation chromatograph, GPC 150-C, manufactured by Waters Ltd. The column

Table II Characteristics of Samples

Sample	MFI (dg/min)	M_n ($\times 10^4$)	M_w ($\times 10^5$)	M_z ($\times 10^6$)	M_{z+1} ($\times 10^6$)	M_w/M_n	M_z/M_w	T_c (°C)
A	0.49	8.02	6.30	2.12	3.95	7.9	3.4	95.5
B	1.73	4.61	4.32	1.69	3.30	9.4	3.9	95
C	4.0	3.53	3.21	1.47	2.89	9.1	4.6	96
D	8.9	2.80	2.66	1.32	2.75	9.5	5.0	96
E	14.7	2.67	2.38	1.27	2.64	8.9	5.3	96.5
F	25.1	1.91	1.86	1.14	2.56	9.8	6.1	102

system used was 10^3, 10^4, 10^5, 10^6, and 10^7 Å and the solvent used was *o*-dichlorobenzene. Although a usual measure of molecular weight distribution, M_w/M_n, scarcely changes with MFI, a measure of molecular weight distribution at high molecular weight range, M_z/M_w, increases with increasing MFI. A thermogram was measured with a sheet about 0.3 mm thick at a cooling rate of 40°C/min using a differential scanning calorimeter, Perkin-Elmer DSC-BI, after melting for 10 min at 230°C in nitrogen gas flow, and the exothermic peak was taken as the crystallization temperature T_c.

Injection Molding

Flexural test specimens (ASTM D790) were injection-molded using an 8 oz Nikko Ankerwerk V22A-120 type reciprocating-screw injection molding machine. The shape of the test specimen is shown in Figure 1. A polymer reservoir was provided to make resin flow in the specimen uniform. The gate size measured 7.0 mm wide, 1.5 mm thick, and 3.0 mm long. The sprue was a truncated cone with 5.4 mm inlet diameter, 7.4 mm outlet diameter, and 45 mm long and the runner measured 7.0 mm wide, 4.5 mm thick, and 100 mm long. Since cylinder temperature affects the degree of molecular orientation of the product and its mechanical properties more than any other injection molding conditions,[28] injection molding was carried out, varying cylinder temperature only and keeping all other conditions constant. Table III lists injection molding conditions adopted. For cylinder temperature, the temperature of the metering zone (MH3) at the extreme end was used.

Structural Analyses

Mean Higher-Order Structures

A thin section about 0.1 mm thick was sliced from the central part of the specimen perpendicular to the flow direction (MD) with a microtome and its crystalline texture was observed with a polarizing microscope, Olympus PM-6, under a magnification of 20×. The thicknesses of the skin layers of both surfaces were averaged.

A wide-angle X-ray diffraction pattern was taken at the central part of the specimen by setting its MD in accord with the meridian using a Rigaku Denki RU-200 diffractometer with Ni-filtered Cu-K_α radiation at a sample-to-film distance of 45 mm. Using a goniometer, a 2θ scan was carried out at a scan speed of 4°/min and azimuthal scans of the (110) and (040) plane reflections were carried out at a scan speed of 8°/min, and crystalline orientation functions f_{a^*}, f_b, and f_c were calculated according to Wilchinsky's method.[29] The a^*-axis-oriented component fraction $[A^*]$ was obtained by the method described in the Results section. A 2θ scan was carried out at the central part of the specimen using a rotating specimen table and the crystallinity X_c was calculated according to Weidinger and Hermans' method.[30]

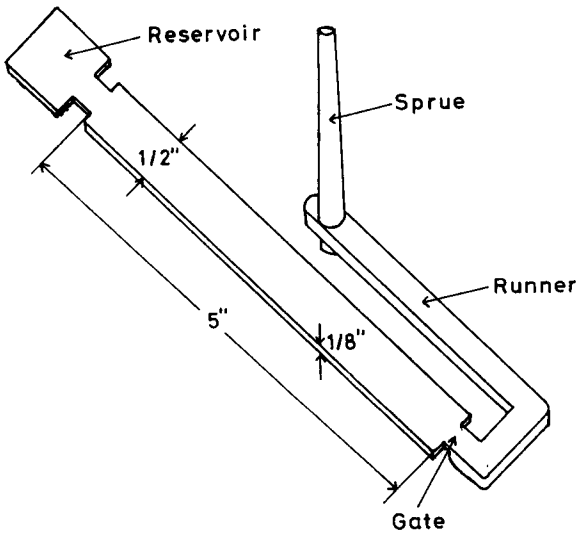

Figure 1 Shape of test specimen.

Table III Injection Molding Conditions

Expt No.	Cylinder Temperature (°C) MH1[a]	MH2[b]	MH3[c]	DH[d]	Injection Pressure (kg/cm^2)	Injection Speed (cc/s)	Mold Temperature (°C)	Cooling Time (s)
1	160	190	200	190	500	13.5	40	40
2	160	220	240	220	500	13.5	40	40
3	160	250	280	250	500	13.5	40	40
4	160	280	320	280	500	13.5	40	40

[a] Feed zone.
[b] Compression zone.
[c] Metering zone.
[d] Die head.

These measurements were carried out on all specimens molded from each resin at each cylinder temperature.

Distribution of Higher-Order Structures in Flow Direction

Since the length of the specimen was about 12.7 cm, X_c, thickness of the skin layer, $[A^*]$, and crystalline orientation functions at the parts 2.1, 4.2, 6.3, 8.4, and 10.5 cm far from the gate were measured by the methods described in the previous section.

These measurements were carried out on specimens molded from each sample at a cylinder temperature of 240°C and specimens molded from the B sample at each cylinder temperature.

Distribution of Higher-Order Structures in Thickness Direction

X_c, $[A^*]$, and the crystalline orientation functions were measured by the methods described in the previous section on thin sections about 0.3 mm thick, sliced successively from the surface to the center parallel to the surface at the central parts of specimens molded from each sample at a cylinder temperature of 240°C and of specimens molded from the B sample at each cylinder temperature and at five parts in the flow direction of a specimen molded from the B sample at a cylinder temperature of 240°C. Wide-angle X-ray diffractograms were measured on the same sections using the rotating specimen table and the β-crystal contents, K values, were obtained according to Turner-Jones et al.'s method.[31]

RESULTS

Mean Higher-Order Structures

Figure 2 shows the dependence of crystallinity X_c on the cylinder temperature. A tendency is seen that X_c increases with increasing MFI and cylinder temperature. It is a general tendency that X_c of a compression-molded article increases with increasing MFI in the case of the same molding conditions.[32] The fact that X_c increases with increasing cylinder temperature is because the higher the cylinder temperature, the higher the injected resin temperature, which takes a longer time to be cooled and the cooling rate is low.

Figure 3 exemplifies the changes caused by cylinder temperature to a crystalline texture observed with a polarizing microscope and a wide-angle X-ray diffraction pattern for the B sample. The polarizing micrographs show clear skin/core structures. The thickness of the skin layer decreases with increasing cylinder temperature. Also, c-axis and a^*-axis mixed orientations are seen in the wide-angle X-ray diffraction patterns and the degree of orientation of crystalline molecular chains decreases with increasing cylinder temperature.

Figure 4 shows the dependence of the thickness

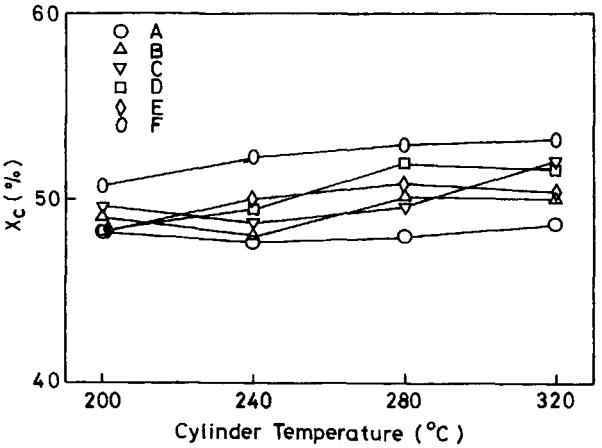

Figure 2 Dependence of crystallinity X_c on cylinder temperature.

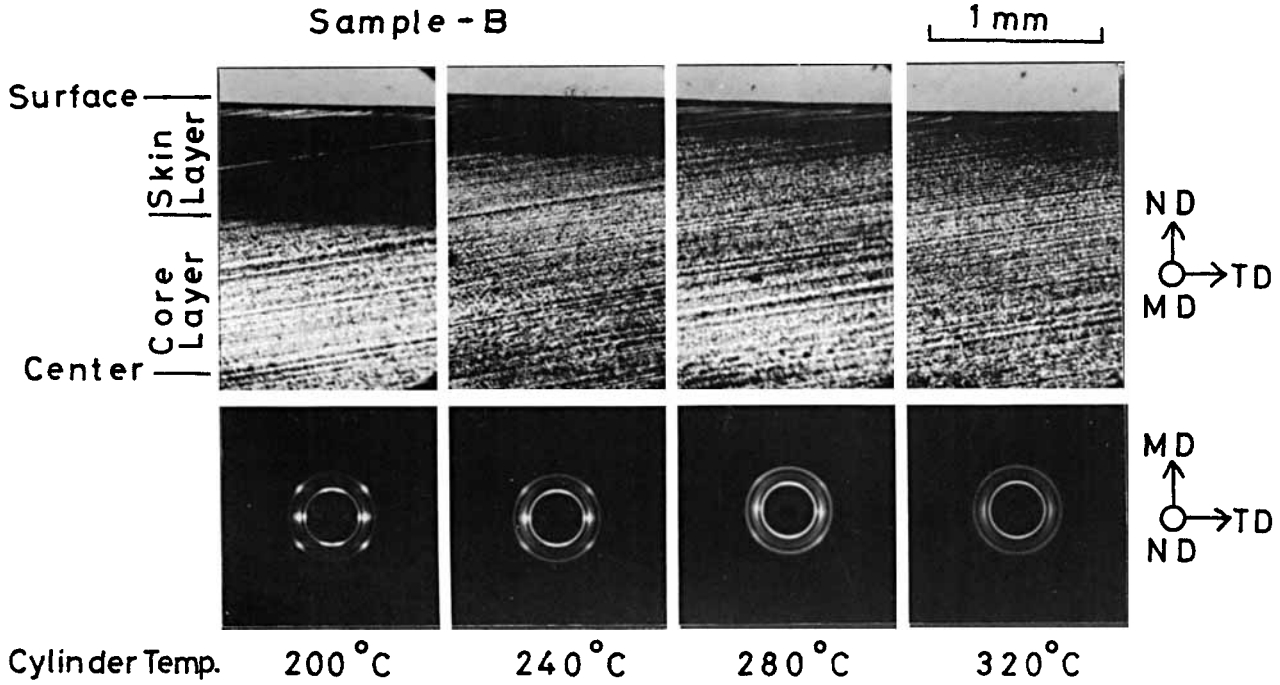

Figure 3 Changes with cylinder temperature, of polarized micrograph and wide-angle X-ray diffraction pattern. B sample.

of the skin layer on cylinder temperature. The thickness of the skin layer decreases with increasing cylinder temperature and comparison at the same cylinder temperature indicates that the thickness decreases in proportion as MFI is high.

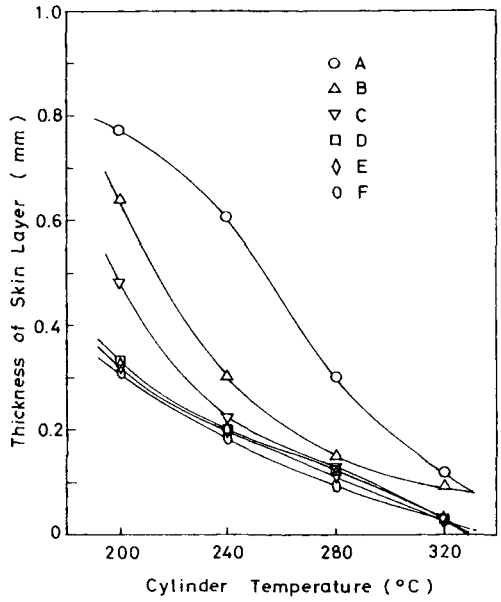

Figure 4 Dependence of thickness of skin layer on cylinder temperature. Influence of MFI of resin.

Figure 5 exemplifies the 2θ scan curve and (110) plane and (040) plane azimuthal scan curves of a specimen molded from the B sample at a cylinder temperature of 240°C. Here, in order to evaluate the proportions of the c-axis-oriented component and a^*-axis-oriented component, the following procedure is carried out: A base line (BL2) is drawn horizontally at the bottom of the azimuthal scan curve of the (110) reflection; the area around an azimuthal angle of 0° above the base line is taken as C and the area around the azimuthal angle of 90° above the base line is taken as A^*; the c-axis-oriented component fraction $[C]$ and a^*-axis-oriented component fraction $[A^*]$ are defined as follows:

$$[C] = \frac{C}{C + A^*} \tag{1}$$

$$[A^*] = \frac{A^*}{C + A^*} \tag{2}$$

Although there is no assurance that the absolute amounts of c-axis-oriented and a^*-axis-oriented components can be rigorously evaluated by $[C]$ and $[A^*]$, a relative comparison may be made by them when raw resin and/or molding conditions are changed. Also, the crystalline orientation functions (a^*-axis orientation function f_{a^*}, b-axis orientation

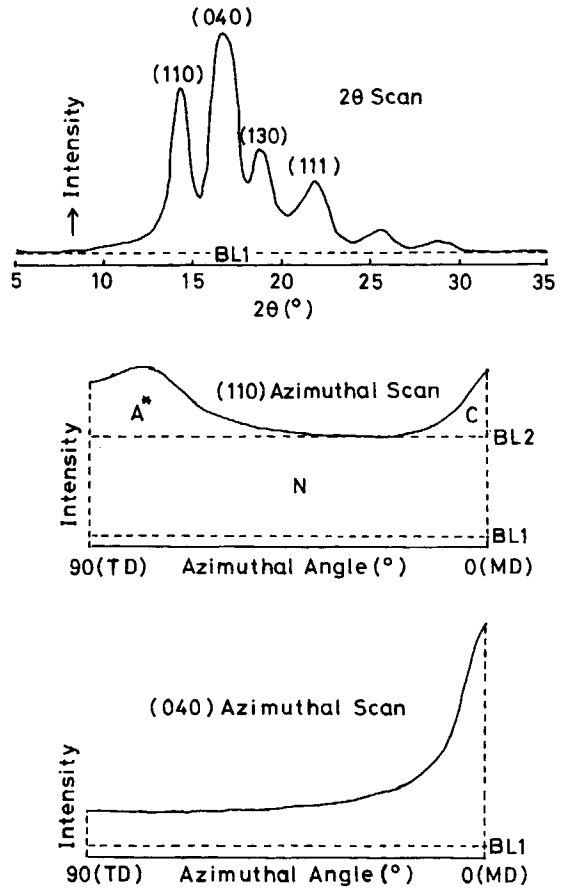

Figure 5 (a) 2θ scan curve. (b) (110) plane azimuthal scan curve. (c) (040) plane azimuthal scan curve. B sample. Cylinder temperature 240°C.

function f_b, and c-axis orientation function f_c) were calculated from the (110) plane and (040) plane azimuthal scan curves according to Wilchinsky's method.[29]

Figure 6 shows the dependence of the a^*-axis-oriented component fraction $[A^*]$ on cylinder temperature. A tendency is seen that $[A^*]$ increases with increasing MFI and cylinder temperature. Namely, it means that the fraction of the a^*-axis-oriented component as against to that of the c-axis-oriented component increases with increasing MFI and cylinder temperature.

Figure 7 shows the dependence of the orientation functions on cylinder temperature. The absolute values of the c-axis orientation function f_c and b-axis orientation function f_b decrease with increasing cylinder temperature and comparison at the same cylinder temperature indicates that these values are small in proportion as MFI is high. a^*-Axis orientation function f_{a^*} somewhat increases with increasing cylinder temperature and depends little on MFI.

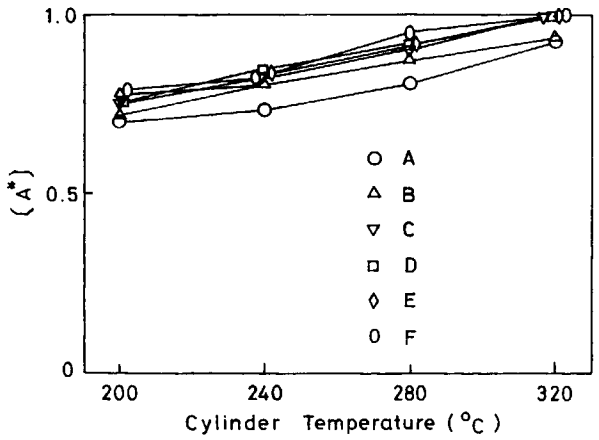

Figure 6 Dependence of a^*-axis-oriented component fraction $[A^*]$ on cylinder temperature. Influence of MFI of resin.

β-Crystal content could be not evaluated since the reflection intensity of wide-angle X-ray diffraction of β-crystals was weak.

Distribution of Higher-Order Structures in Flow Direction

Figure 8 shows the distributions in the flow direction of crystallinities X_c of specimens molded from each sample at a cylinder temperature of 240°C and Fig-

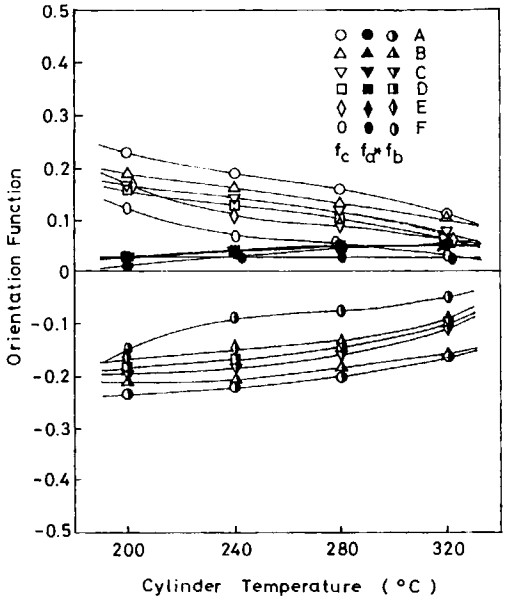

Figure 7 Dependences of crystalline orientation functions on cylinder temperature. Influence of MFI of resin.

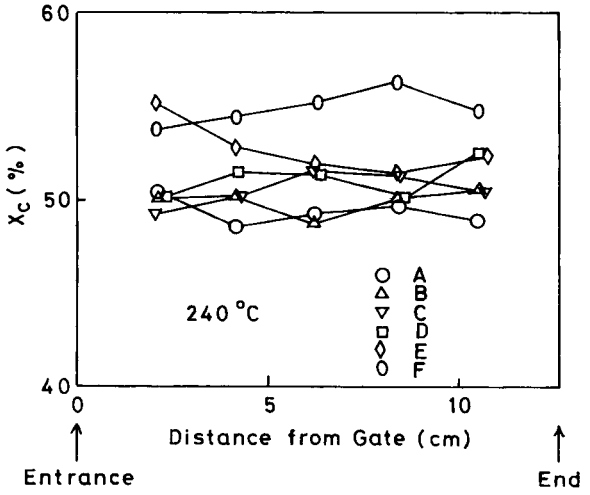

Figure 8 Distribution of crystallinity X_c in flow direction. Influence of MFI of resin. Cylinder temperature 240°C.

ure 9 shows those of specimens molded from the B sample at each cylinder temperature. As a large tendency, X_c increases with increasing MFI of resin[32] and scarcely depends on cylinder temperature and distance from the gate. Trotignon et al.[8] measured by X-ray diffraction the distribution of crystallinity X_c in the flow direction of a tensile test specimen injection-molded from a polypropylene and found that X_c was very high near the gate, decreased once, and showed a maximum at around the center. Murphy et al.[21,22] reported that X_c, measured by X-ray diffraction, of an injection-molded polypropylene rectangular plate was higher as the molecular weight of polypropylene was higher and cylinder temperature was lower and decreased with

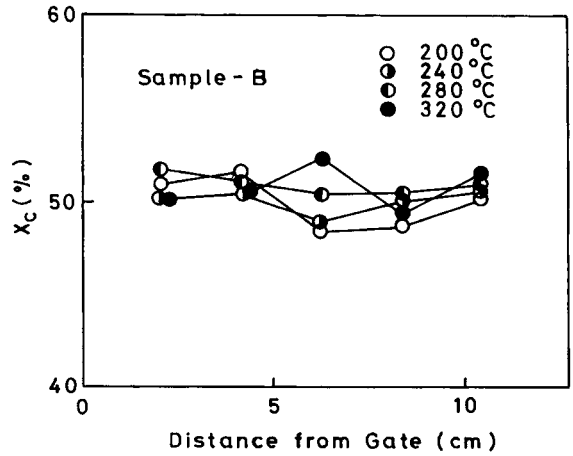

Figure 9 Distribution of crystallinity X_c in flow direction. Influence of cylinder temperature. B sample.

going away from the gate. Menges et al.[17,24] reported that X_c's, obtained from density, of injection-molded polypropylene angle bar and square plate decreased with going away from the gate. The present results differ from these results, whose reason is not obvious at the present time.

Figures 10 and 11 shows the distributions of the thickness of the skin layer in the flow direction. The thickness of the skin layer is higher as MFI and cylinder temperature are lower and decreases with going away from the gate. The decreasing rate of the thickness of the skin layer in the flow direction increases with going away from the gate and with increasing MFI and cylinder temperature. Altendorfer and Seitl[10] observed a similar tendency. Krsova[5] also observed a similar tendency. However, in his results, the decreasing rate of the thickness of the skin layer in the flow direction was very high and increased with increasing the molecular weight of polypropylene resin. The difference between the decreasing rate behavior in the present results and that in Krsova's results is assumed to be because although our mold cavity had a reservoir, his cavity had no reservoir. Hirose et al.,[7] Altendorfer et al.,[9,11] Koppelmann et al.,[15,23] and Menges et al.[17] reported that the thickness of the skin layer showed a maximum near the gate. Although no maximum is ob-

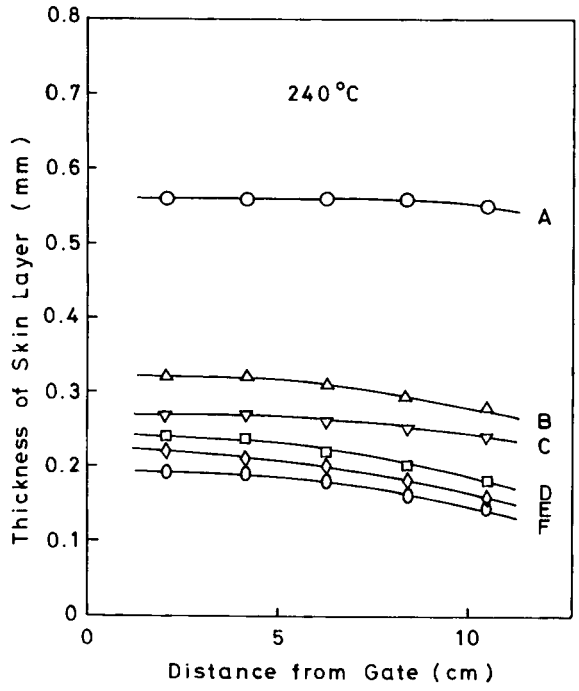

Figure 10 Distribution of thickness of skin layer in flow direction. Influence of MFI of resin. Cylinder temperature 240°C.

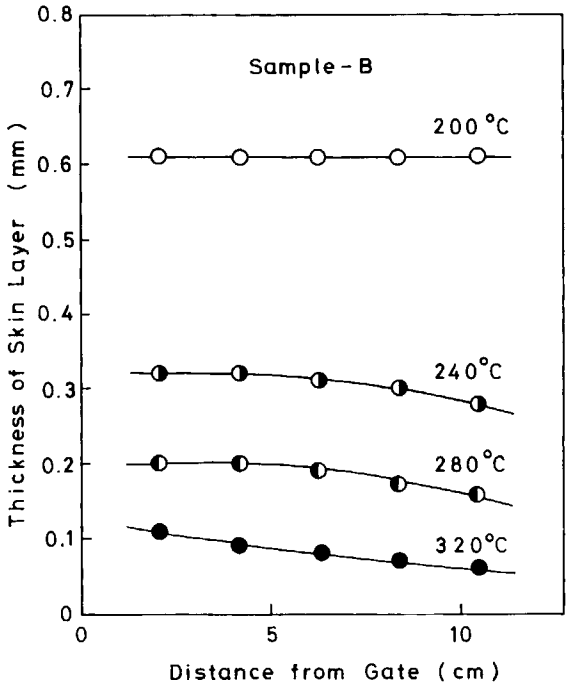

Figure 11 Distribution of thickness of skin layer in flow direction. Influence of cylinder temperature. B sample.

served near the gate in the present experiment, there is almost no decrease in the thickness of the skin layer near the gate.

Figures 12 and 13 show the distributions of the a^*-axis-oriented component fraction $[A^*]$ in the flow direction. $[A^*]$ is higher as MFI and cylinder temperature are higher and increases with going away from the gate. The present study is the first that evaluates $[A^*]$.

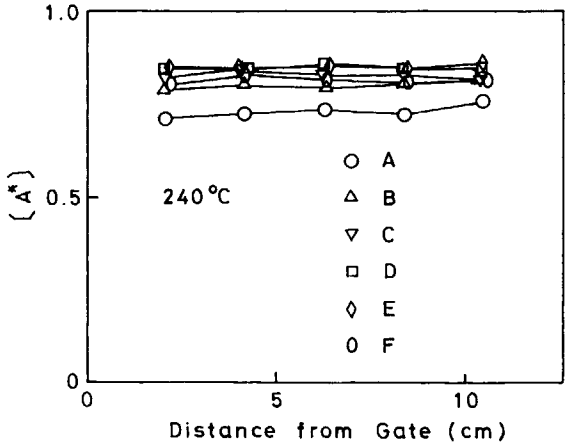

Figure 12 Distribution of a^*-axis-oriented component fraction $[A^*]$ in flow direction. Influence of MFI of resin. Cylinder temperature 240°C.

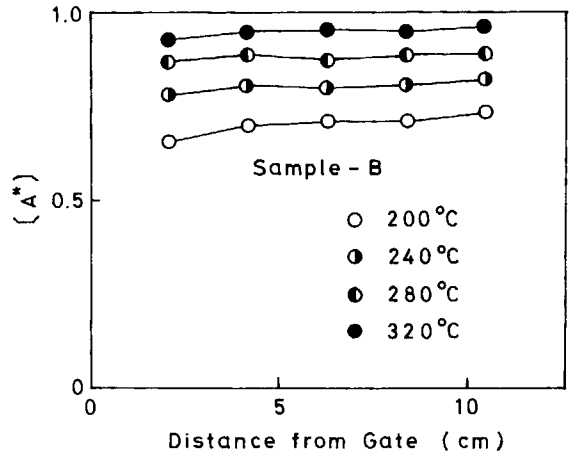

Figure 13 Distribution of a^*-axis-oriented component fraction $[A^*]$ in flow direction. Influence of cylinder temperature. B sample.

Figure 14 exemplifies the distributions in the flow direction of the c-axis orientation function f_c, a^*-axis orientation function f_{a^*}, and b-axis orientation function f_b of a specimen molded from the B sample at a cylinder temperature of 240°C. The absolute values of f_c, f_{a^*}, and f_b decrease with going away from the gate. Similar tendencies were obtained for specimens molded from other samples at other cylinder temperatures. However, f_{a^*} increases with going away from the gate for specimens with high molecular orientation such as the specimen molded from the A sample at a cylinder temperature of 240°C and the specimen molded from the B sample at a cylinder temperature of 200°C.

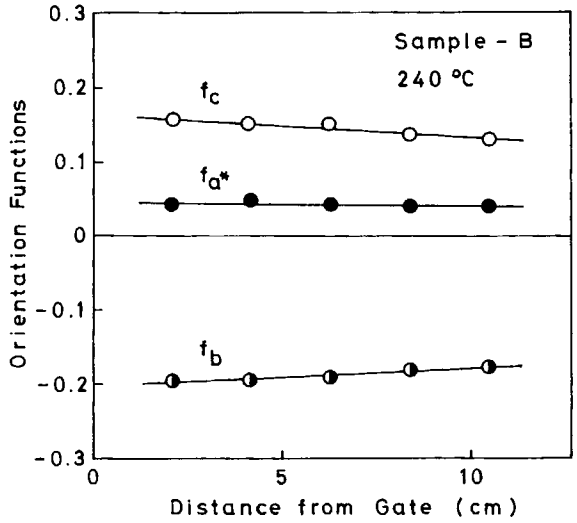

Figure 14 Distributions of crystalline orientation functions in flow direction. B sample. Cylinder temperature 240°C.

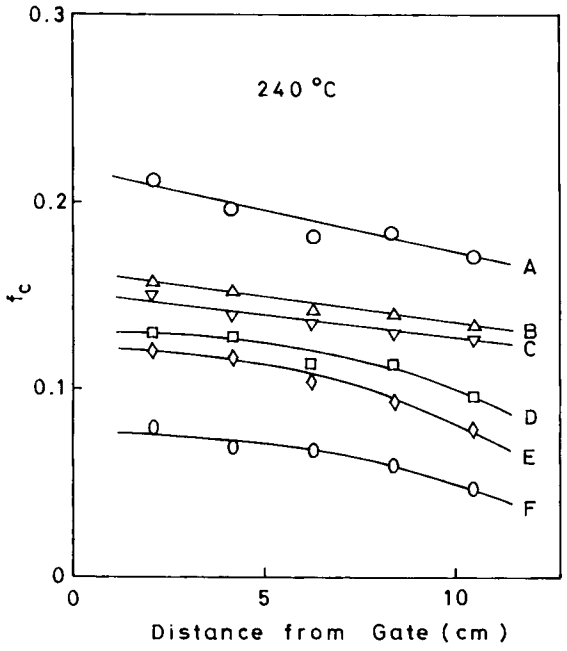

Figure 15 Distribution of c-axis orientation function f_c in flow direction. Influence of MFI of resin. Cylinder temperature 240°C.

Figures 15 and 16 show the distributions of the c-axis orientation function f_c in the flow direction. f_c is higher as MFI and cylinder temperature are lower and decreases with going away from the gate.

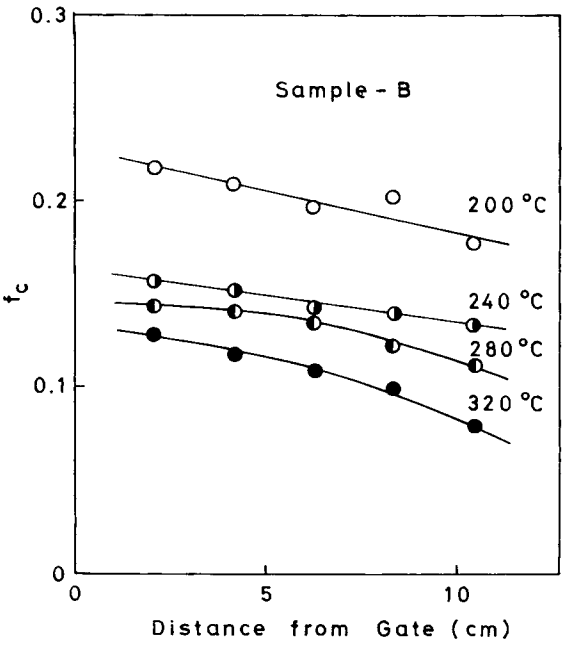

Figure 16 Distribution of c-axis orientation function f_c in flow direction. Influence of cylinder temperature. B sample.

The decreasing rate of f_c in the flow direction increases with going away from the gate and with increasing MFI and cylinder temperature. Trotignon et al.[8,13,14] observed a similar tendency on the crystalline orientation A, which was obtained from the (110) and (111) plane reflection intensities in X-ray diffraction and on the crystalline and amorphous orientations, f_{cr}, and f_{am}, measured by infrared dichroism. Murphy et al.[21,22] also obtained similar results on A. Altendorfer and Seitl[10] and Menges et al.[17,24] obtained similar results on the orientation degree measured by birefringence. Kubota[18] reported that the orientation degree measured by fluorescence showed a maximum at a midway part in the flow direction of a rectangular plate.

Since the reflection intensity by the β-crystals was weak, the distribution of β-crystal content in the flow direction could not be evaluated.

Distribution of Higher-Order Structures in Thickness Direction

Figures 17–19 show the distributions of crystallinity X_c in the thickness direction. Here, H is half of the thickness of specimen and y is the distance from the center. X_c is low at the surface region and increases toward the interior. This is because the inner region

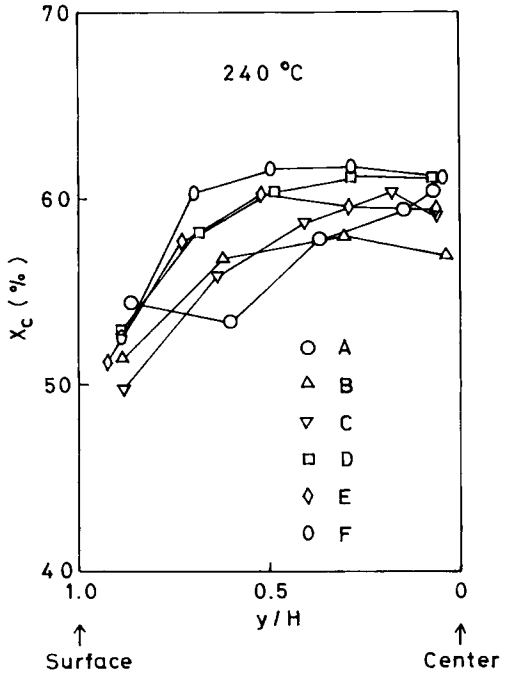

Figure 17 Distribution of crystallinity X_c in thickness direction. Influence of MFI of resin. Cylinder temperature 240°C.

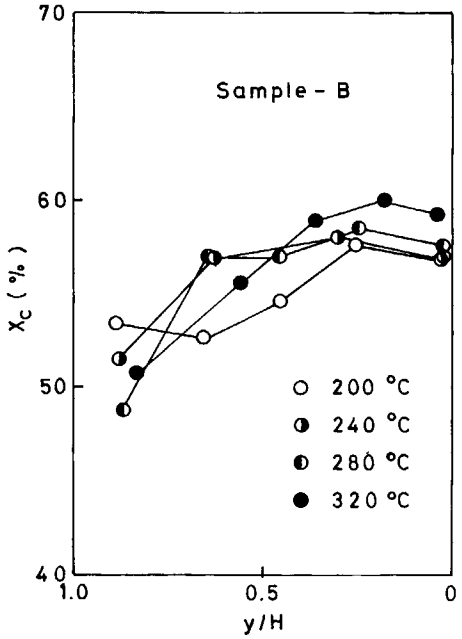

Figure 18 Distribution of crystallinity X_c in thickness direction. Influence of cylinder temperature. B sample.

is cooled more slowly. A similar tendency was reported by Houska and Brumell[19,20] on X_c's measured by infrared spectrum and density. Their results show that X_c shows a minimum at the surface skin region and increases toward the interior. Trotignon and Verdu[13,14] obtained X_c from the heat of fusion measured by differential scanning calorimetry, which showed, contrary to the Houska et al.'s results, a maximum at the skin region, decreased once, and increased toward the interior. Since our, Houska et al.'s, and Trotignon et al.'s results differ in the measuring method of X_c, they cannot be absolutely compared, particularly at the surface region of specimen where the degree of molecular orientation is high. However, they agree in the point that X_c increases toward the interior in the inner region where the degree of molecular orientation is low. Although a clear tendency is not observed on the influences of cylinder temperature (Fig. 18) and distance from the gate (Fig. 19), as for the influence of MFI (Fig. 17), it seems that X_c is higher as MFI is higher[32] over the whole range across the thickness direction as a large tendency. The point nearest the surface of the specimen molded from the A sample at a cylinder temperature of 240°C and the point nearest the surface of the specimen molded from the B sample at a cylinder temperature of 200°C show rather high X_c. This is assumed to be because these specimens have thick skin layers and high degrees of molecular orientation at the surface regions.

Figures 20–22 show the distributions of the β-crystal content, K value, in the thickness direction. Except for the surface regions of the specimen

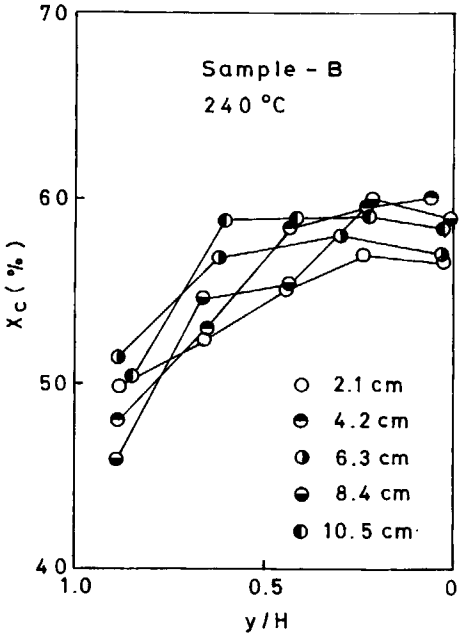

Figure 19 Distribution of crystallinity X_c in thickness direction. Influence of position in flow direction. B sample. Cylinder temperature 240°C.

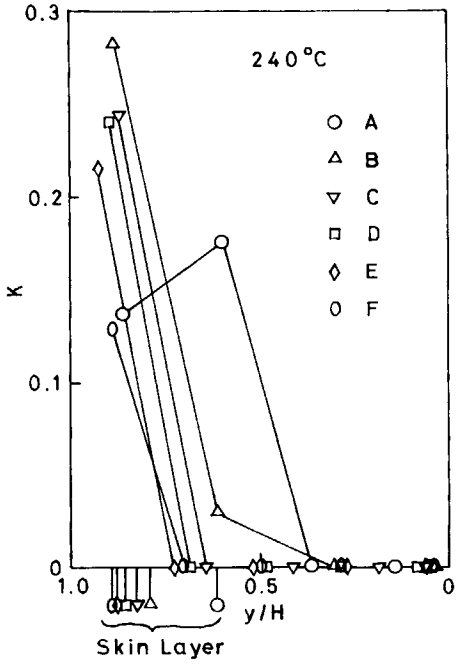

Figure 20 Distribution of β-crystal content, K value, in thickness direction. Influence of MFI of resin. Cylinder temperature 240°C.

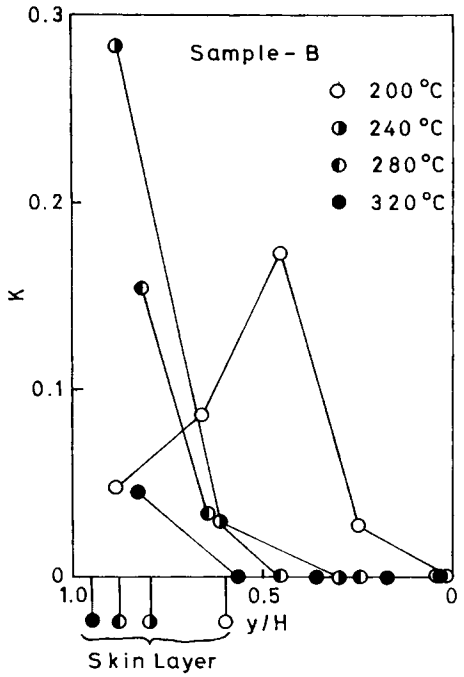

Figure 21 Distribution of β-crystal content, K value, in thickness direction. Influence of cylinder temperature. B sample.

molded from the A sample at a cylinder temperature of 240°C and the specimen molded from the B sample at a cylinder temperature of 200°C, the K value is higher nearer the surface and decreases toward the interior. As seen from Figures 20 and 21, the K value is generally higher as MFI and cylinder temperature are lower. Figure 22 shows that the distribution of the β-crystal content in the thickness direction is nearly uniform across the flow direction. The skin regions are shown in Figures 20 and 21, which show that the K value is high at the region of about twice the thickness of the skin layer and that β-crystals exist at the surface region of about twice the thickness of the skin layer. As can be seen from the cases of the A sample molded at a cylinder temperature of 240°C and the B sample molded at a cylinder temperature of 200°C, it seems that there exist not so much β-crystals at the surface skin region and the β-crystals exist most at the region inside the skin layer. Kantz et al.[1] found that the β-crystals existed in the shear zones inside the skin layer of injection-molded polypropylene. Fitchmun and Mencik[2] found from polarizing microscopy that the β-crystals existed at the boundary between oriented layer (layer 3) and core layer. Trotignon and Verdu[13] also found that the β-crystal content was maximum at the region inside the skin layer. Since β-crystals reduce the impact strength of injection-molded polypropylene,[21,22] it is desirable to suppress their formation to the utmost.

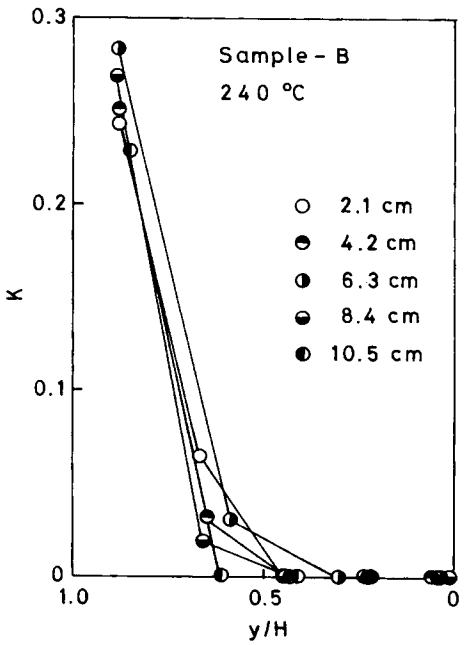

Figure 22 Distribution of β-crystal content, K value, in thickness direction. Influence of position in flow direction. B sample. Cylinder temperature 240°C.

Figures 23–25 show the distriubtions of the a^*-axis-oriented component fraction $[A^*]$ in the thickness direction. In these figures, since the degree of molecular orientation is very low around the central region, there is some problem in evaluating $[A^*]$ and the precision of $[A^*]$ is not good around the central region. $[A^*]$ increases toward the interior; there is little c-axis-oriented component and most crystals show the a^*-axis orientation at $y/H < 0.5$.

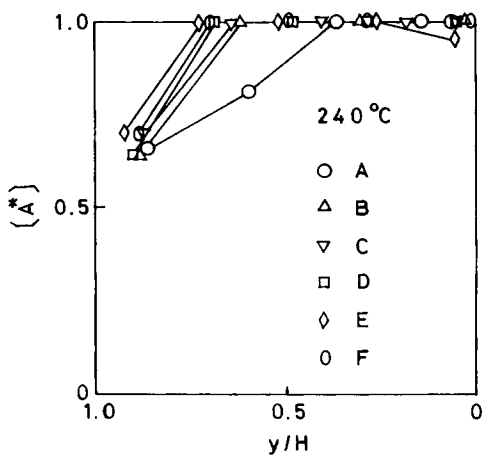

Figure 23 Distribution of a^*-axis-oriented component fraction $[A^*]$ in thickness direction. Influence of MFI of resin. Cylinder temperature 240°C.

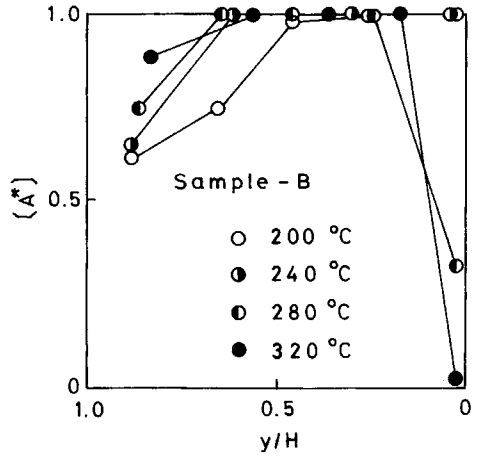

Figure 24 Distribution of a^*-axis-oriented component fraction $[A^*]$ in thickness direction. Influence of cylinder temperature. B sample.

$[A^*]$ is higher as MFI and cylinder temperature are higher. Figure 25 shows that the distribution of $[A^*]$ in the thickness direction scarcely changes in the flow direction.

Figure 26 exemplifies the distributions in the thickness direction, of the crystalline orientation functions of a specimen molded from the B sample at a cylinder temperature of 240°C. The absolute values of f_c and f_b are higher nearer the surface and f_{a^*} shows a maximum at a midway region. Similar results were obtained on the specimens molded from other samples at other cylinder temperatures. The distributions of crystalline orientation functions have been studied on injection-molded high density polyethylenes by Kamal and Moy.[33-35]

Figures 27–29 show the distributions of the c-axis orientation function f_c in the thickness direction. f_c is higher nearer the surface and is higher as MFI and cylinder temperature are lower at around the surface region. Figure 29 shows that the distri-

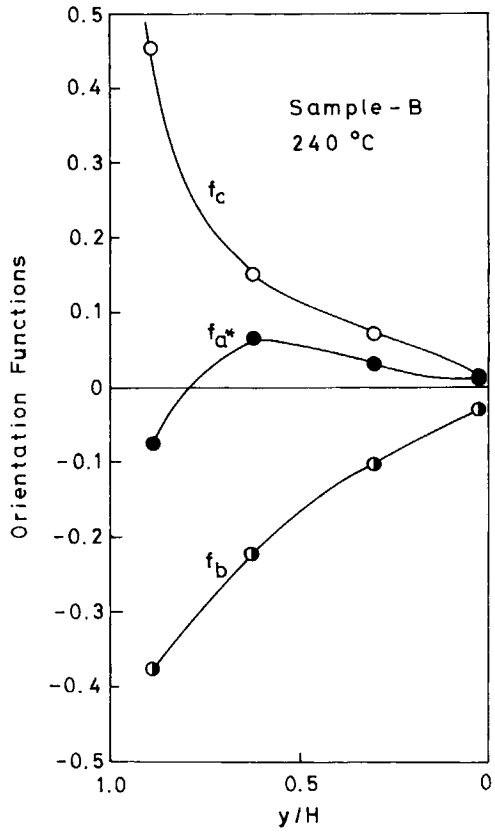

Figure 26 Distributions of crystalline orientation functions in thickness direction. B sample. Cylinder temperature 240°C.

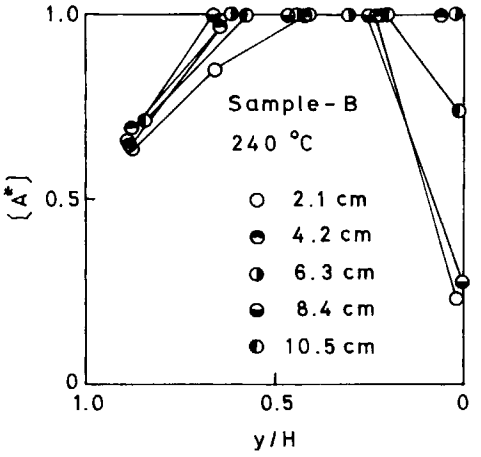

Figure 25 Distribution of a^*-axis-oriented component fraction $[A^*]$ in thickness direction. Influence of position in flow direction. B sample. Cylinder temperature 240°C.

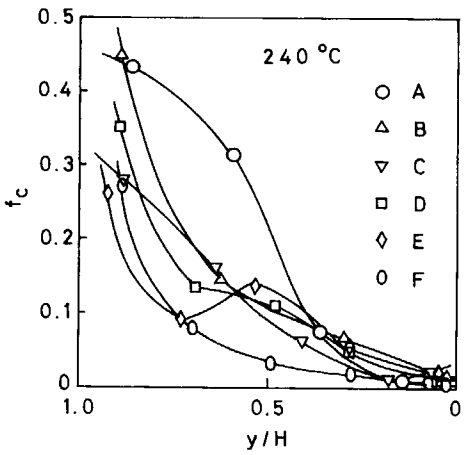

Figure 27 Distribution of c-axis orientation function f_c in thickness direction. Influence of MFI of resin. Cylinder temperature 240°C.

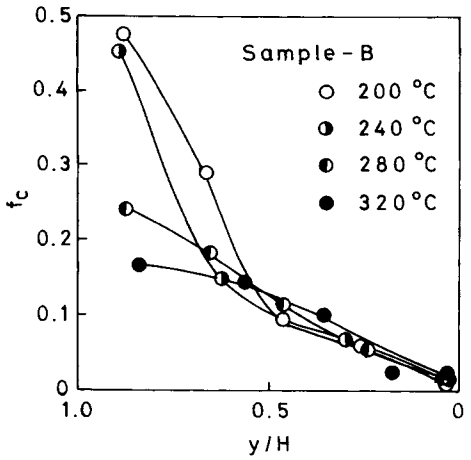

Figure 28 Distribution of c-axis orientation function f_c in thickness direction. Influence of cylinder temperature. B sample.

bution of f_c in the thickness direction is nearly uniform across the flow direction. A peak and a shoulder are observed at $y/H \simeq 0.5$, respectively, on the specimen molded from the E sample at a cylinder temperature of 240°C and on the specimen molded from the D sample at a cylinder temperature of 240°C, which are assumed to be caused by the secondary flow during the cooling and pressure holding process. Koppelmann et al.[15,16,23] measured the distributions in the thickness direction, of birefringences of injecton-molded polypropylenes, and found that birefringences at the inner regions of specimens molded with holding pressures were higher than that molded without holding pressure. Hirose et al.,[7] Koppelmann et al.,[15,16,23] and Menges et al.[17] measured the distribution of birefringence in the thickness direction, Trotignon and Verdu[13,14] measured the distribution in the thickness direction, of orientation degree A by X-ray diffraction, and Trotignon and Verdu[13] and Houska and Brumell[19,20] measured the distributions in the thickness direction, of crystalline and amorphous orientation functions f_{cr} and f_{am} by infrared dichroism. They all observed a maximum of molecular orientation around the surface region. In the present experiment, however, as a possible reason, due to a large slicing interval, no such maximum was observed and f_c decreased gradually from the surface to the interior. Kubota[18] measured the distribution of the degree of fluorescent orientation in the thickness direction and found that no orientation maximum was observed around the surface region and the degree of orientation decreases gradually from the surface to the interior as in the present results. Kamal et al.[12] measured on an injection molding of polypropylene filled with 10 wt % glass fibers the distributions in the thickness direction, of the content and orientation state of glass fibers, and the distributions in the flow and thickness directions, of the degrees of crystalline and amorphous orientations by infrared dichroism. As a result, they found that crystalline molecular chains were oriented perpendicular to the flow direction and the degree of the orientation was higher nearer the gate and surface and was increased by the filling of glass fibers. Furthermore, they found that amorphous molecular chains were oriented to the flow direction and the degree of the orientation was higher nearer the gate and surface and was increased by the filling of glass fibers.

DISCUSSION

As mentioned above, the influences of MFI of polypropylene and cylinder temperature on the distributions of higher-order structures such as crystallinity X_c, β-crystal content K, a^*-axis-oriented component fraction $[A^*]$, thickness of skin layer, and crystalline c-axis orientation function f_c in injection-molded polypropylenes were studied. Ones out of these higher-order structures, which most influence the product properties such as mechanical and thermal properties, are the degrees of molecular orientation such as the thickness of the skin layer and f_c. Therefore, next we will make theoretical consideration on the molecular orientation in injection molding.

Many studies have so far been carried out on the molecular orientation process in plastics injection

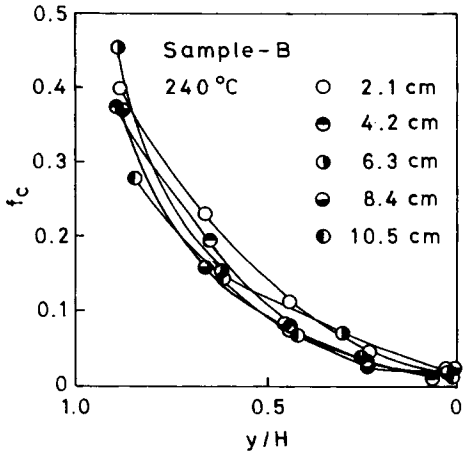

Figure 29 Distribution of c-axis orientation function f_c in thickness direction. Influence of position in flow direction. B sample. Cylinder temperature 240°C.

molding.[28,36–57] The authors regarded recoverable shear strain as a measure of molecular orientation in melt and analyzed the molecular orientation process in injection molding of polypropylene from a viewpoint of growth of a recoverable shear strain at the gate and its relaxation in the cavity.[28,42,51–53] Since the variations of molecular orientation in the flow and thickness directions were not studied in detail in our previous papers and the theory was after that revised on the value of recoverable shear strain and the treatment of relaxation time of recoverable shear strain, the revised theory and experimental results will be described again.

Theory

In injection molding, a molten resin passes through the sprue, runner, and gate, fills the cavity, and becomes a shaped article through cooling and solidification. In the meantime, the extent of melt orientation changes at the different parts. As shown in the Experimental section, the cross section of the flow path at the gate is extremely small, compared with the sprue, runner, and cavity and the flow rate is constant throughout the flow path. Therefore, the shear rate at the gate is extremely high and most of the melt orientation takes place during passage through the gate.

In this analysis, recoverable shear strain γ_e is used as a measure of the melt orientation. As shown in Figure 30, the recoverable shear strain having grown during passage through the gate, γ_{e0}, undergoes a Maxwell-type relaxation with a relaxation time λ_1 while flowing through the cavity and becomes γ_{e1}.

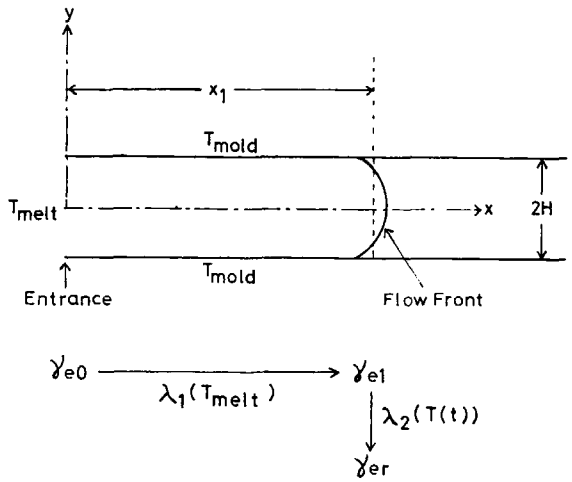

Figure 30 Coordinates and movements of recoverable shear strain γ_e in mold cavity.

At this time, cooling is ignored until the resin completely fills the cavity, and the resin temperature is regarded as identical to the injected resin temperature T_{melt}. Therefore, it is regarded that, meanwhile, a relaxation occurs with the relaxation time $\lambda_1(T_{melt})$ at the injected resin temperature T_{melt}. Then, the resin at a certain position x_1 from the gate is cooled by the mold at the temperature T_{mold} and its temperature becomes $T(t)$. The recoverable shear strain γ_{e1} undergoes a temperature-dependent Maxwell-type relaxation with a relaxation time $\lambda_2(T(t))$ and becomes a residual recoverable shear strain γ_{er} when the resin temperature reaches a crystallization temperature T_c. γ_{er} is assumed to be proportional to the degree of orientation of an injection-molded article.

With V for the injection rate, B for the width of the cavity, and $2H$ for the thickness of the cavity, time t_1 taken by the flow to reach the position x_1 from the inlet of the cavity is expressed by

$$t_1 = 2BHx_1/V \tag{3}$$

Then, γ_{e1} is calculated by

$$\gamma_{e1} = \gamma_{e0} \exp\left[\frac{-t_1}{\lambda_1(T_{melt})}\right] = \gamma_{e0} \exp\left[\frac{-2BHx_1}{V\lambda_1(T_{melt})}\right] \tag{4}$$

Here, the Carslaw–Jaeger equation for one-dimensional non-steady-state thermal conduction of infinite solid[58] is applied, ignoring the latent heat of crystallization. Then, the time change of the resin temperature $T(t)$ at y $(0 \le y \le H)$ from the center in the thickness direction is expressed by

$$\frac{T - T_{mold}}{T_{melt} - T_{mold}} = 2\sum_{n=0}^{\infty} \frac{(-1)^n}{\pi(n+\frac{1}{2})} \cos\left[(n+\tfrac{1}{2})\frac{\pi y}{H}\right] \times \exp\left[-(n+\tfrac{1}{2})^2\pi^2\frac{\alpha t}{H^2}\right] \tag{5}$$

where α is the thermal diffusivity.

If eq. (5) is rewritten in the form of $t = f(T)$, the residual recoverable shear strain γ_{er} is calculated by

$$\ln\frac{\gamma_{er}}{\gamma_{e1}} = -\int_{T_{melt}}^{T_c} \frac{1}{\lambda_2(T)}\frac{df(T)}{dT}\,dT \tag{6}$$

Half of the cavity thickness, H, is divided into 10 equal parts, the residual recoverable shear strain at

the center of each division, $\gamma_{er,i}$, is calculated by eq. (6), and the mean residual recoverable shear strain γ_{er} is calculated by

$$\gamma_{er} = \frac{1}{10}\sum_{i=1}^{10}\gamma_{er,i} \tag{7}$$

The material characteristics needed to calculate γ_{er} are the initial recoverable shear strain γ_{e0}, its relaxation times λ_1, λ_2, the thermal diffusivity α, and the crystallization temperature T_c.

Experimental

Measurements of Rheological Properties

Recoverable Shear Strain. The recoverable shear strain γ_e was obtained by measuring capillary flow property. According to Heron et al.,[59] the recoverable shear strain in die flow consists of two components: One is the entrance component γ_e(entrance) which grows at the die inlet and the other is the transient component γ_e(transient) which grows in the die land. γ_e(transient) is expressed by[59]

$$\gamma_e(\text{transient}) \simeq \dot{\gamma}_c\lambda(\dot{\gamma}_c)\{1 - \exp[-t_c/\lambda(\dot{\gamma}_c)]\} \tag{8}$$

where $\dot{\gamma}_c$ is the shear rate in the die, $\lambda(\dot{\gamma}_c)$ is the relaxation time at the shear rate of $\dot{\gamma}_c$, and t_c is the residence time in the die. $\lambda(\dot{\gamma}_c)$ is expressed by

$$\lambda(\dot{\gamma}_c) \simeq \lambda_0\frac{\eta(\dot{\gamma}_c)}{\eta_0} \tag{9}$$

where λ_0 is the relaxaton time at the shear rate of 0, $\eta(\dot{\gamma}_c)$ is the shear viscosity at the shear rate of $\dot{\gamma}_c$, and η_0 is the zero-shear viscosity.

γ_e(entrance) was obtained from the end correction coefficient in capillary flow. The relation between pressure P and volumetric flow rate Q was measured with a Koka flow tester manufactured by Shimazu Seisakusho Co., Ltd. at temperatures of 200, 240, 280, and 320°C, which were in accord with the cylinder temperatures in injection molding. The dies used were three straight dies with radius R = 0.25 mm, length L = 1.0, 2.5, and 5.0 mm, and L/R = 4, 10, and 20.

The apparent shear rate $\dot{\gamma}'_w$, the true shear rate $\dot{\gamma}_w$, and the effective shear stress τ_w at the wall in the capillary flow of a viscoelastic fluid are given by eqs. (10), (11), and (12), respectively:

$$\dot{\gamma}'_w = \frac{4Q}{\pi R^3} \tag{10}$$

$$\dot{\gamma}_w = \frac{\dot{\gamma}'_w}{4}\left(3 + \frac{d\log\dot{\gamma}'_w}{d\log\tau_w}\right) \tag{11}$$

$$\tau_w = \frac{(P - P_c - P_e)R}{2L} \tag{12}$$

$$= \frac{PR}{2(L + n_cR + eR)} \tag{12'}$$

$$= \frac{PR}{2(L + \nu R)} \tag{12''}$$

$$\nu = n_c + e \tag{13}$$

where P_c and P_e are the pressure loss caused by the contraction of flow at the capillary inlet and the pressure loss caused by the elastic deformation, respectively. n_cR and eR are capillary lengths corresponding to P_c and P_e, respectively, and n_c is the Couette correction term. According to Philippoff and Gaskins,[60] $2e$ is equal to the recoverable shear strain γ_e(entrance). Namely,

$$\nu = n_c + \frac{\gamma_e(\text{entrance})}{2} \tag{14}$$

Rearranging eq. (12''),

$$P = 2\tau_w(L/R) + 2\nu\tau_w \tag{15}$$

A rectilinear relationship should be obtained if pressure P needed to produce a definite shear stress τ_w and hence a definite shear rate $\dot{\gamma}'_w$ is plotted against L/R (Bagley plot[61]), and the end correction coefficient ν is obtained as an intercept of the L/R axis.

γ_e(transient) was obtained as follows: The true shear rate $\dot{\gamma}_w$ and the effective shear stress τ_w were calculated by eqs. (11) and (12), respectively, and the shear viscosity $\eta(\dot{\gamma}_c)$ was calculated by $\eta(\dot{\gamma}_c) = \tau_w/\dot{\gamma}_w$. γ_e(transient) was calculated by eqs. (9) and (8) from $\eta(\dot{\gamma}_c)$, the zero-shear viscosity η_0 [Fig. 37(a)], and the zero-shear relaxation time λ_0 [Fig. 37(b)], the last two of which were obtained in the following section.

Relaxation Time. The relaxation time λ was obtained from the absolute value of complex viscosity, $|\eta^*(\omega)|$, according to Graessley's method.[62] Graessley showed experimentally that, regardless of the type of polymer and temperature, there is a relationship of

$$\dot{\gamma}_0\eta_0 J_e^0 = 0.6 \pm 0.2 \qquad (16)$$

among $\dot{\gamma}_0$, the shear rate at which the shear viscosity $\eta(\dot{\gamma})$ lowers to 0.8 times the zero-shear viscosity η_0, and η_0 and the steady-state shear compliance J_e^0. Since $\eta(\dot{\gamma})$ and $|\eta^*(\omega)|$ are equivalent functions in a range of low $\dot{\gamma}$ and ω,[63] the characteristic relaxation time $\lambda_0 = \eta_0 J_e^0$ can be calculated, using ω_0, the angular frequency at the time when $|\eta^*(\omega)|$ is $0.8\eta_0$, in place of $\dot{\gamma}_0$ in eq. (16). Equation (16) shows that there is a standard deviation of ± 0.2 depending on the kind of polymer. However, here, 0.6 was used for the right-hand side term of eq. (16) since the subject was only polypropylenes.

Measurements of Thermal Properties

Thermal Diffusivity. Thermal diffusivity α was obtained by calculation from document data. For thermal conductivity k, a constant value of 5.0×10^{-4} cal/cm s °C was used for both solid and molten states according to Matsumoto et al.'s solid-state value of 4.5×10^{-4} cal/cm s °C[64] and Fuller and Fricke's molten-state value of 5.0×10^{-4} cal/cm s °C.[65] Density ρ was calculated from Danusso et al.'s empirical formulae concerning the temperature changes of specific volumes v_c and v_a of, respectively, crystalline and amorphous polypropylenes.[66] Specific heat C_p was calculated from Gee and Melia's empirical formulae.[67] Thermal diffusivity α is calculated from k, ρ, and C_p by $\alpha = k/\rho C_p$. The temperature change of α calculated in this way is shown in Figure 31. The value of α does not greatly change at temperatures encountered by a resin in injection molding. Therefore, $\alpha = 1.03 \times 10^{-3}$ cm^2/s, value at 200°C was used for calculations in orientation analysis.

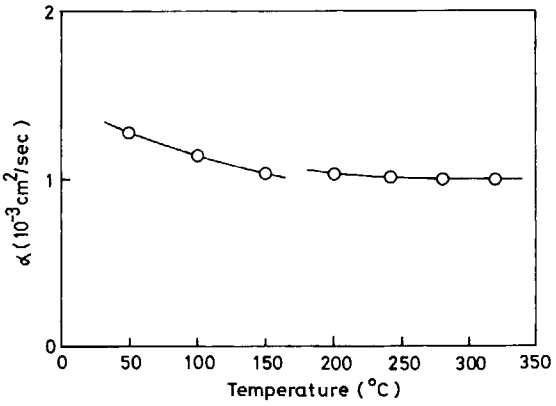

Figure 31 Temperature change of thermal diffusivity α of polypropylene.

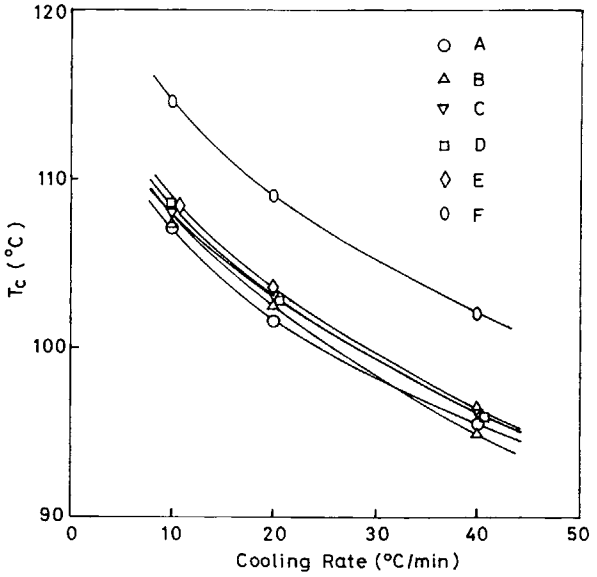

Figure 32 Dependence of crystallization temperature T_c on cooling rate.

Crystallization Temperature. A thermogram was measured with a sheet about 0.3 mm thick at cooling rates of 10, 20, and 40°C/min using a differential scanning calorimeter, Perkin Elmer DSC-BI, after melting for 10 min at 230°C in the nitrogen gas flow, and the exothermic peak was taken as crystallization temperature T_c. As shown in Figure 32, T_c decreases with increasing cooling rate. For calculations in the analysis of the orientation process, T_c at a cooling rate of 40°C/min was used, as shown in Table II, in consideration of high cooling rate met in injection molding.

Experimental Results

Recoverable Shear Strain

Figure 33 exemplifies apparent flow curves expressed in the form of the apparent shear rate $\dot{\gamma}'_w$ vs. pressure P, of the B sample measured at 240°C using various L/R dies. The Bagley plots carried out, using Figure 33, are shown in Figure 34. Fine Bagley plots were obtained for all samples at all temperatures.

Figure 35(a) exemplifies the change with $\dot{\gamma}'_w$ of the end correction coefficient ν obtained from Bagley plots for the B sample. ν tends to decrease as temperature rises but ν at 280°C and that at 320°C are reversed. A similar tendency was obtained with all other samples except for the F sample.

According to Bagley,[68] Hook's law of the following expression holds:

$$\tau_w = \mu\gamma_e(\text{entrance}) \qquad (17)$$

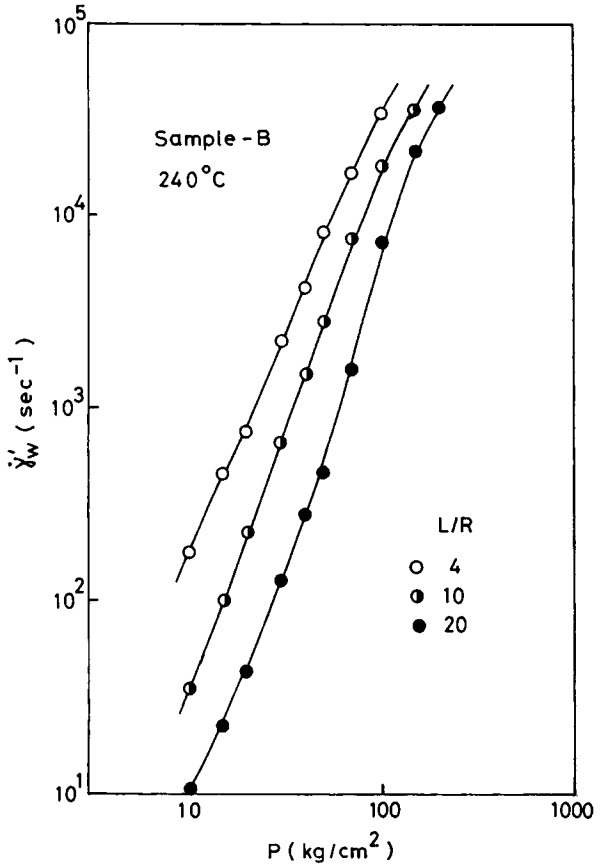

Figure 33 Apparent flow curves measured with dies of various L/R, expressed in the form of apparent shear rate $\dot{\gamma}'_w$ vs. pressure P. B sample measured at 240°C.

where τ_w is shear stress, μ is shear modulus, and γ_e(entrance) is the entrance component of recoverable shear strain.

If eq. (17) is substituted into eq. (14),

$$\nu = \frac{\tau_w}{2\mu} + n_c \qquad (18)$$

Therefore, if the end correction coefficient ν is plotted against shear stress τ_w, a rectilinear relationship should be obtained and the Couette's correlation term n_c is obtained from an intercept of the ν-axis. The recoverable shear strain γ_e(entrance) was obtained by substituting into eq. (14) n_c, which had been obtained by plotting ν against τ_w and extrapolating τ_w into 0, where the effective shear stress τ_w had been calculated by eq. (12″), using ν, which had been obtained from the Bagley plots. Figure 35(b) exemplifies the change of γ_e(entrance) with $\dot{\gamma}'_w$ for the B sample. γ_e(entrance) increases with increasing $\dot{\gamma}'_w$ and decreases as temperature rises. A similar tendency was observed with all other samples.

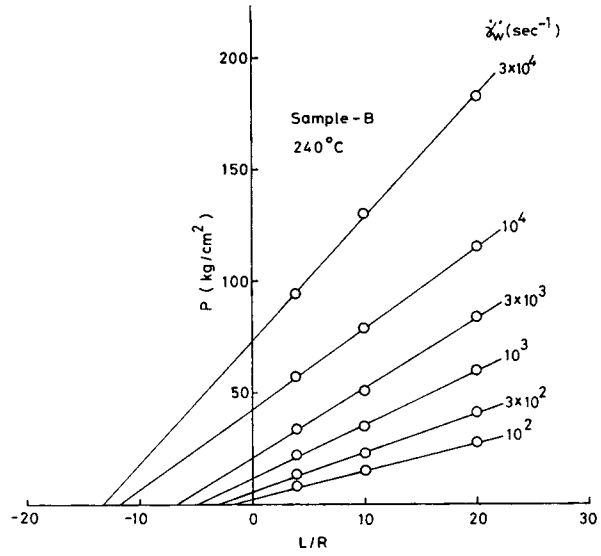

Figure 34 Bagley plots; B sample; 240°C.

Apparent shear rate $\dot{\gamma}'_w$ at the wall in slit flow is given by the following equation[69]:

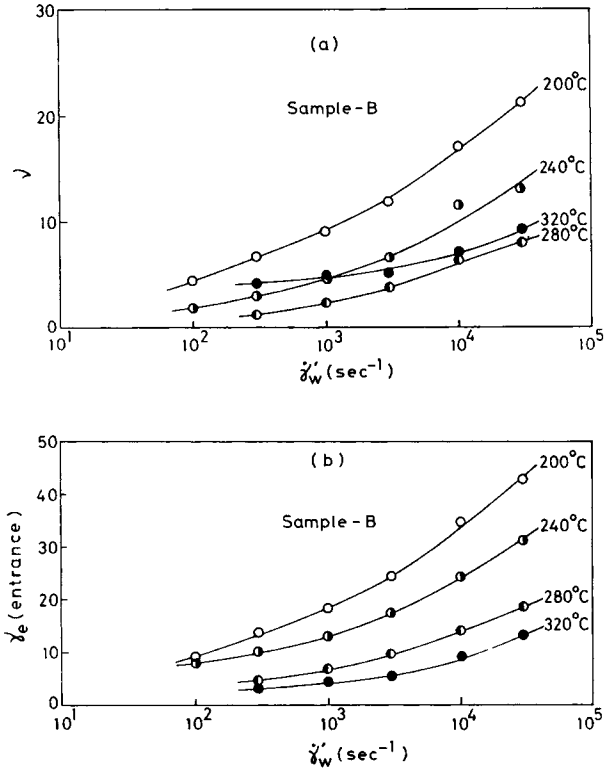

Figure 35 (a) End correction coefficient ν vs. apparent shear rate $\dot{\gamma}'_w$. (b) Entrance component of recoverable shear strain, γ_e (entrance) vs. apparent shear rate $\dot{\gamma}'_w$. B sample.

$$\dot{\gamma}'_w = \frac{6Q}{(2H)^2(B + 2H)} \qquad (19)$$

where Q is the volumetric flow rate, $2H$ is the thickness of the slit, and B is its width. If the shear rate at the gate in injection molding under this experiment is calculated using eq. (19), $\dot{\gamma}'_w \fallingdotseq 4200\ s^{-1}$. Then, γ_e(entrance) at $\dot{\gamma}'_w = 4200\ s^{-1}$ can be taken as the initial recoverable shear strain γ_{e0}(entrance) mentioned in the previous section. The temperature change of γ_{e0}(entrance) is shown in Figure 36. γ_{e0}(entrance) tends to decrease as temperature and the MFI of resin increase.

On the other hand, the transient component of recoverable shear strain, γ_{e0}(transient), was calculated using eqs. (8) and (9). It scarcely depended on the kind of resin and temperature and had a value of about 9.2. Then, total initial recoverable shear strain γ_{e0} was obtained by the following equation:

$$\gamma_{e0} = \gamma_{e0}(\text{entrance}) + \gamma_{e0}(\text{transient}) \qquad (20)$$

Relaxation Time

Figure 37(a) shows the temperature change of the absolute value of complex viscosity, $|\eta^*(\omega)|$, of the B sample while Figure 37(b) shows $|\eta^*(\omega)|$ of each sample measured at 200°C. It is seen that behaviors of from Newtonian flow to non-Newtonian flow appear.

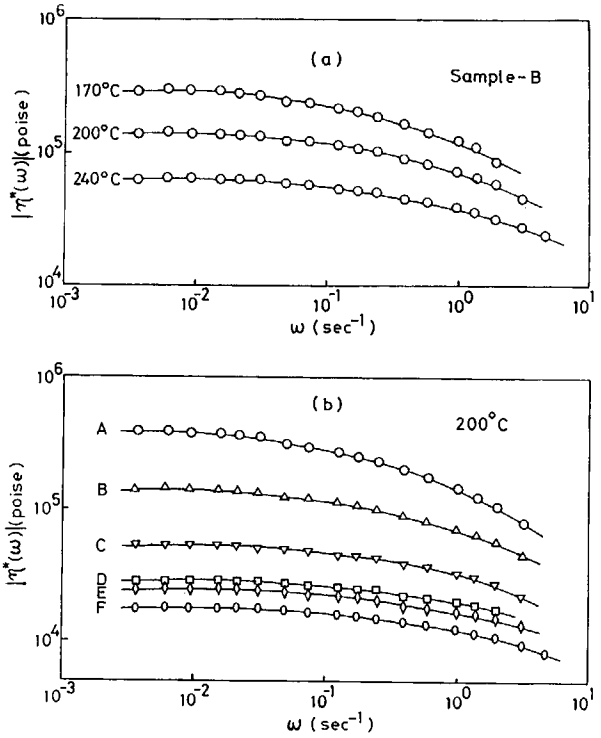

Figure 37 (a) Absolute values of complex viscosities, $|\eta^*(\omega)|$, of B sample at various temperatures. (b) Absolute values of complex viscosities, $|\eta^*(\omega)|$, of various samples at 200°C.

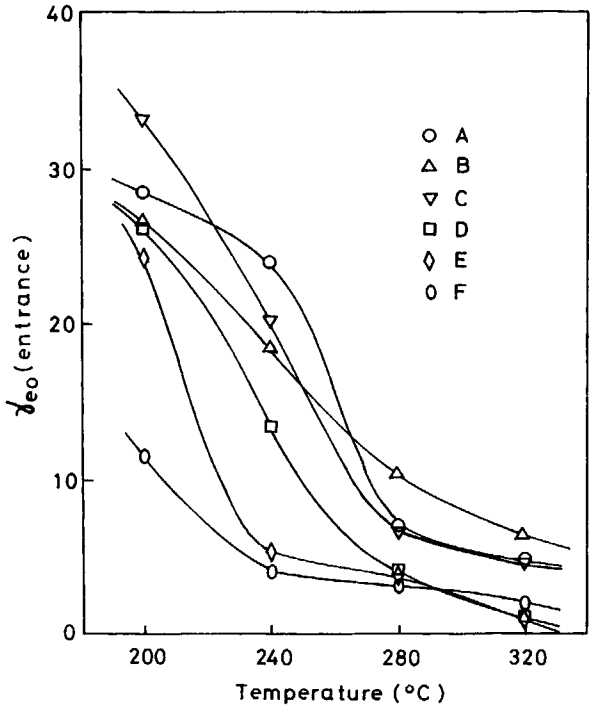

Figure 36 Temperature change of entrance component of initial recoverable shear strain, γ_{e0} (entrance).

Figures 38(a) and (b) show the temperature changes of, respectively, the zero-shear viscosity η_0 and the characteristic relaxation time λ_0 which was obtained by Graessley's method. η_0 and λ_0 obey the Arrhenius equation and the apparent activation energies are almost the same among samples at about 10.0 and 5.7 kcal/mol, respectively. Therefore, $\lambda_1(T)$ and $\lambda_2(T)$ mentioned in the Theory section are given in the form of

$$\lambda_{1,2}(T) = A \exp\left(\frac{B}{T + 273}\right) \qquad (21)$$

where A and B are constants independent of temperature.

Analysis of Molecular Orientation Process

Figure 39 shows the change of resin temperature T with position in the thickness direction, y/H, and time t, calculated by eq. (5). Here, T is expressed

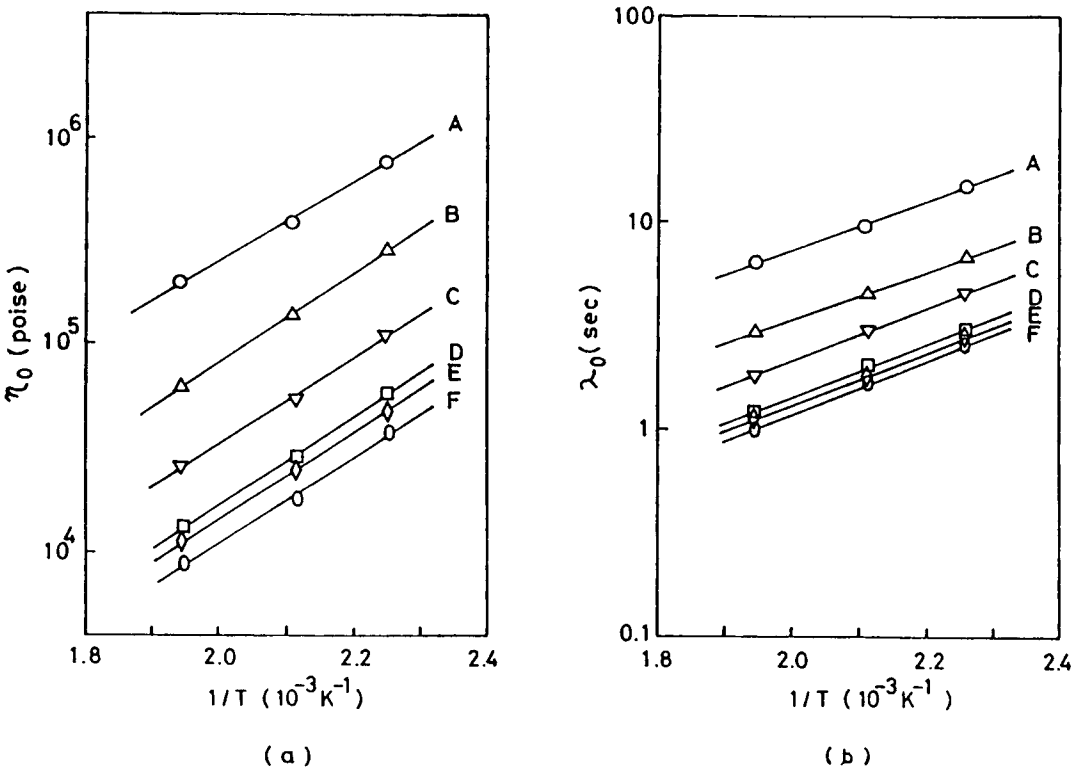

Figure 38 Arrhenius plots of (a) zero-shear viscosity η_0 and (b) characteristic relaxation time λ_0.

by a nondimensional quantity of $(T - T_{mold})/(T_{melt} - T_{mold})$. As a matter of course, cooling rate is higher nearer the surface of large y/H.

The shear rate in the mold cavity, calculated by eq. (19), is about 500 s^{-1}, which means that flow in the mold cavity is sufficiently in the nonlinear region. Since there is possibility that the relaxation time in nonlinear flow is shorter than the relaxation

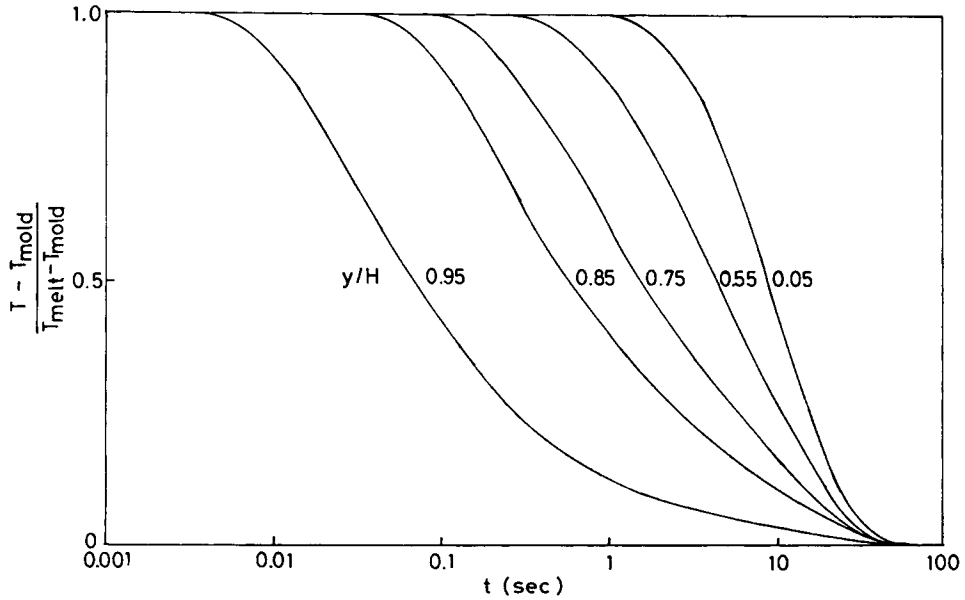

Figure 39 Variations of resin temperatures T at various thicknesswise positions y/H with time t.

time in linear flow region, λ_0,[70] at first, we will evaluate the relaxation time in cavity flow, λ_1. Assuming that $\lambda_2 = \lambda_0$, the change of residual recoverable shear strain γ_{er} in the flow direction when $\lambda_1 = \lambda_0$, $\lambda_0/2$, and $\lambda_0/3$ was calculated using eqs. (5), (7), and (21). Figures 40 and 41 exemplify the calculation results when $\lambda_1 = \lambda_0/2$. From these, the slopes of γ_{er} are calculated by

$$\text{slope of } \gamma_{er} = \frac{\gamma_{er}(2.1) - \gamma_{er}(10.5)}{\gamma_{er}(6.3)} \qquad (22)$$

where $\gamma_{er}(2.1)$, $\gamma_{er}(6.3)$, and $\gamma_{er}(10.5)$ are the recoverable shear strains at the positions 2.1, 6.3, and 10.5 cm far from the gate, respectively. Next, by the same manner as in the case of γ_{er}, the slopes of the changes in the flow direction, of the thickness of the skin layer, ST, and the crystalline c-axis orientation function f_c are calculated from the change of ST in the flow direction in Figures 10 and 11 and the changes of f_c in the flow direction in Figures 15 and 16, respectively:

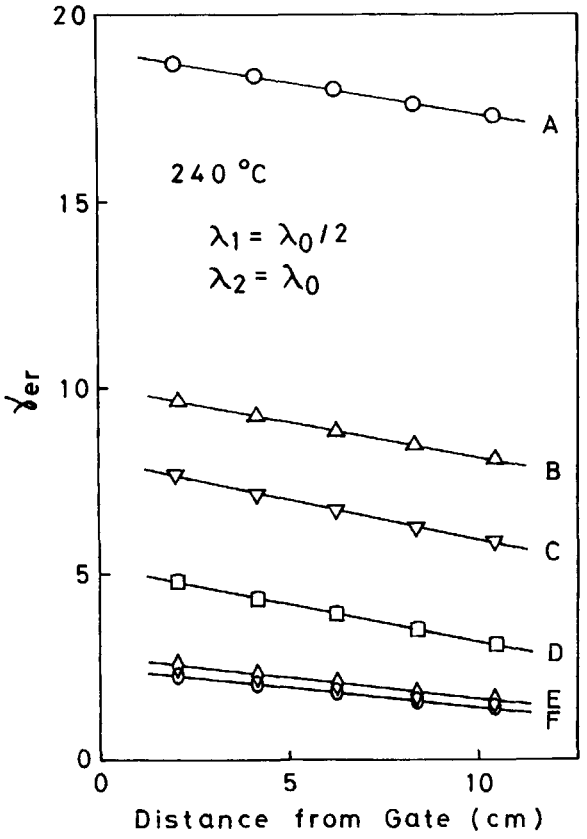

Figure 40 Distribution of calculated mean residual recoverable shear strain γ_{er} in flow direction. Influence of MFI of resin. Cylinder temperature 240°C. $\lambda_1 = \lambda_0/2$, $\lambda_2 = \lambda_0$.

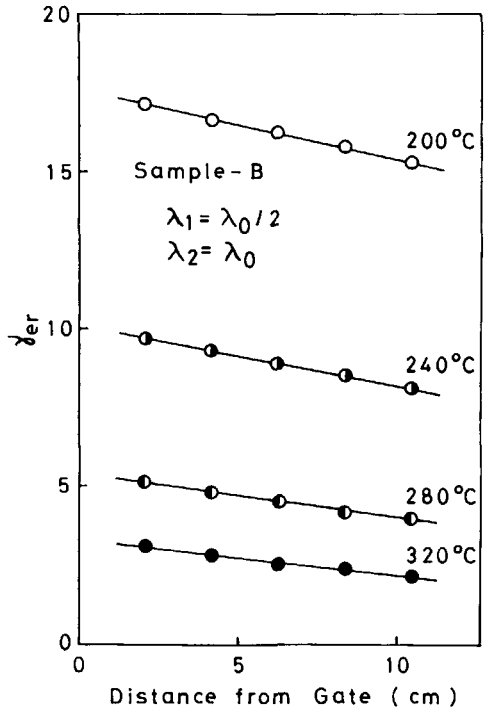

Figure 41 Distribution of calculated mean residual recoverable shear strain γ_{er} in flow direction. Influence of cylinder temperature. B sample. $\lambda_1 = \lambda_0/2$, $\lambda_2 = \lambda_0$.

$$\text{slope of ST} = \frac{\text{ST}(2.1) - \text{ST}(10.5)}{\text{ST}(6.3)} \qquad (23)$$

$$\text{slope of } f_c = \frac{f_c(2.1) - f_c(10.5)}{f_c(6.3)} \qquad (24)$$

Next, the slopes of ST and f_c are plotted against the slope of γ_{er}. These plots are shown in Figure 42, which shows that the slope of correlation is larger than unity when $\lambda_1 = \lambda_0$, the slope is smaller than unity when $\lambda_1 = \lambda_0/3$, and the slopes of measured degrees of molecular orientation such as ST and f_c and that of calculated residual recoverable shear strain γ_{er} are in a proportional relationships with a slope of about unity when $\lambda_1 = \lambda_0/2$. It is conjectured from these results that the relaxation time of recoverable shear strain, λ_1, at the shear rate of 500 s^{-1} in the cavity flow in this experiment is about half of the characteristic relaxation time in linear flow, λ_0. Accordingly, $\lambda_0/2$ is used as λ_1 in the following calculations.

Figure 43 shows how the c-axis orientation function f_c, the thickness of the skin layer, ST, and the calculated mean residual recoverable shear strain γ_{er} change in the flow direction for a flexural specimen molded from the B sample at a cylinder tem-

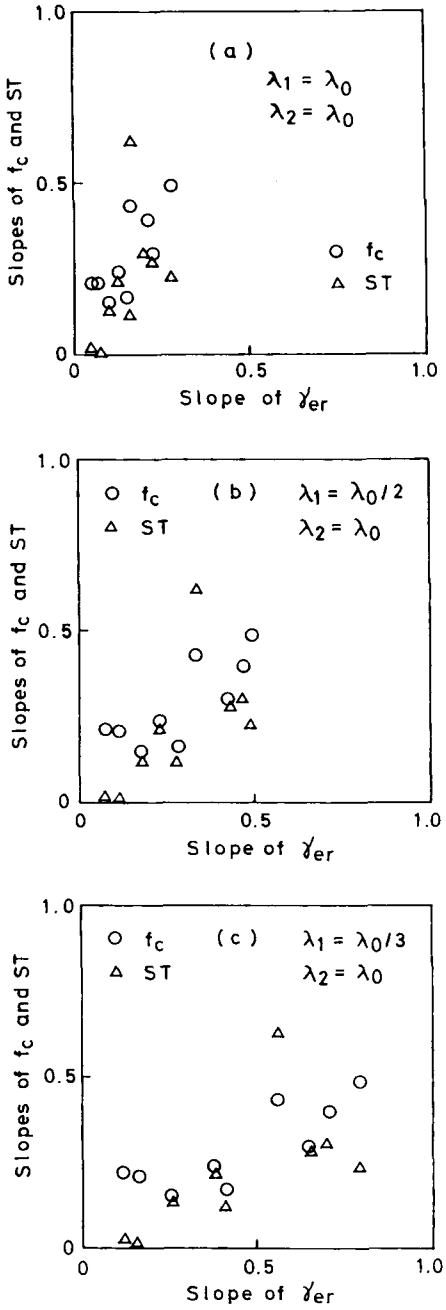

Figure 42 Plots of slopes of c-axis orientation function f_c and thickness of skin layer, ST, in flow direction vs. slope of calculated mean residual recoverable shear strain γ_{er} in flow direction: (a) $\lambda_1 = \lambda_0$; (b) $\lambda_1 = \lambda_0/2$; (c) $\lambda_1 = \lambda_0/3$.

perature of 240°C. ST and f_c decrease in proportion to the distance from the gate and the degrees of these decreases are nearly the same as that of γ_{er}. Similar results were obtained for other samples at other cylinder temperatures.

Figures 44 and 45 show relations between, respectively, the thickness of the skin layer and the

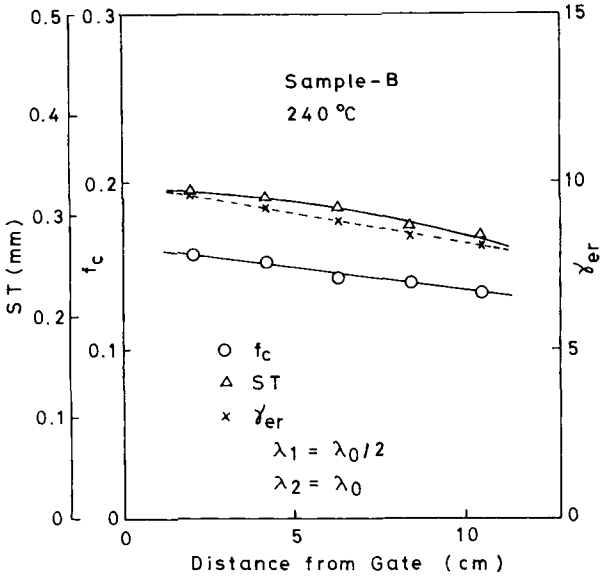

Figure 43 Variations in flow direction of c-axis orientation function f_c, thickness of skin layer, ST, and calculated mean residual recoverable shear strain γ_{er}. B sample. Cylinder temperature 240°C.

c-axis orientation function f_c, and the calculated mean residual recoverable shear strain γ_{er}, at various positions in the flow direction of specimens molded from various samples at various cylinder temperatures. Fairly high correlations exist between the two.

Figure 46 exemplifies a comparison between the

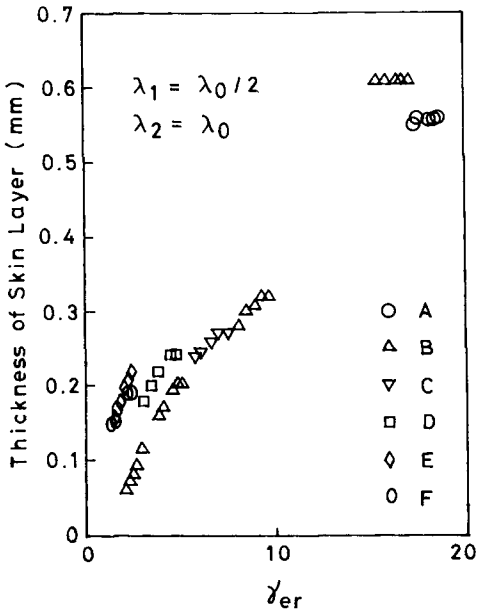

Figure 44 Relation between thickness of skin layer and calculated mean residual recoverable shear strain γ_{er} at various positions in flow direction: $\lambda_1 = \lambda_0/2$, $\lambda_2 = \lambda_0$.

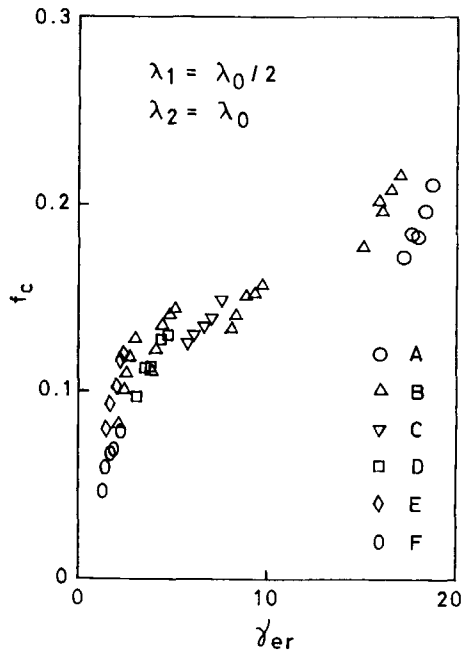

Figure 45 Relation between c-axis orientation function f_c and calculated mean residual recoverable shear strain γ_{er} at various positions in flow direction: $\lambda_1 = \lambda_0/2$, $\lambda_2 = \lambda_0$.

changes in the thickness direction of the c-axis orientation function f_c and the relative residual recoverable shear strain γ_{er}/γ_{e1} calculated using eqs. (5), (6), and (21), for a specimen molded from the B sample at a cylinder temperature of 240°C. The two agree well, thus showing the propriety of using the characteristic relaxation time λ_0 as the relaxation time of recoverable shear strain after cessation of flow in the mold cavity, λ_2.

Figure 47 shows the relation between the c-axis orientation function f_c and calculated residual recoverable shear strain γ_{er} at various positions in the thickness direction of specimens molded from various samples at various cylinder temperatures. Data points n are 65. A fairly high correlation with a correlation coefficient $r = 0.871$ exists between the two.

Figures 48 and 49 show the relation between, respectively, the thickness of the skin layer and the c-axis orientation function f_c and the calculated mean residual recoverable shear strain γ_{er}, at the centers of flexural specimens molded from various samples at various cylinder temperatures. Between the two, fairly high correlations exist regardless of the kind of resin (MFI) and molding conditions (cylinder temperature).

As mentioned above, this theory can considerably well describe not only the mean molecular orientation but also its change in the flow and thickness directions.

CONCLUSION

Flexural test specimens were injection-molded from six homoisotactic polypropylenes with MFI = 0.49–

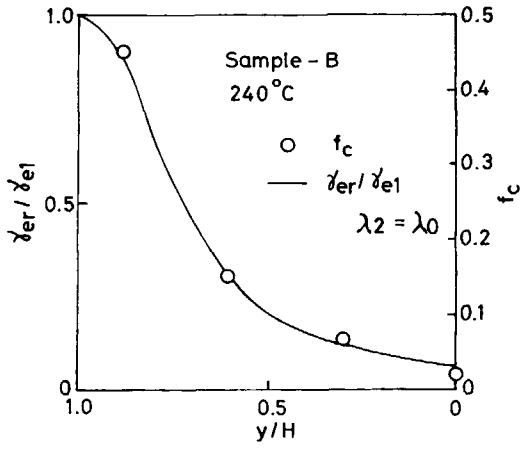

Figure 46 Variations with thicknesswise position y/H of c-axis orientation function f_c and calculated relative residual recoverable shear strain γ_{er}/γ_{e1}. B sample. Cylinder temperature 240°C.

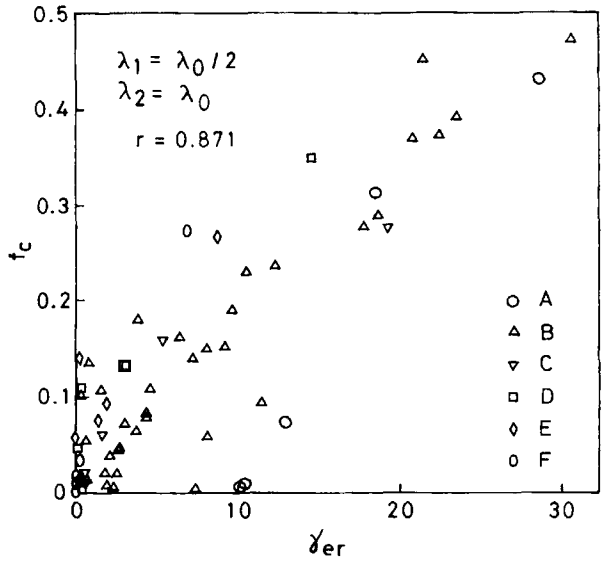

Figure 47 Relation between c-axis orientation function f_c and calculated residual recoverable shear strain γ_{er} at various positions in thickness direction: $\lambda_1 = \lambda_0/2$, $\lambda_2 = \lambda_0$. Data points $n = 65$, correlation coefficient $r = 0.871$.

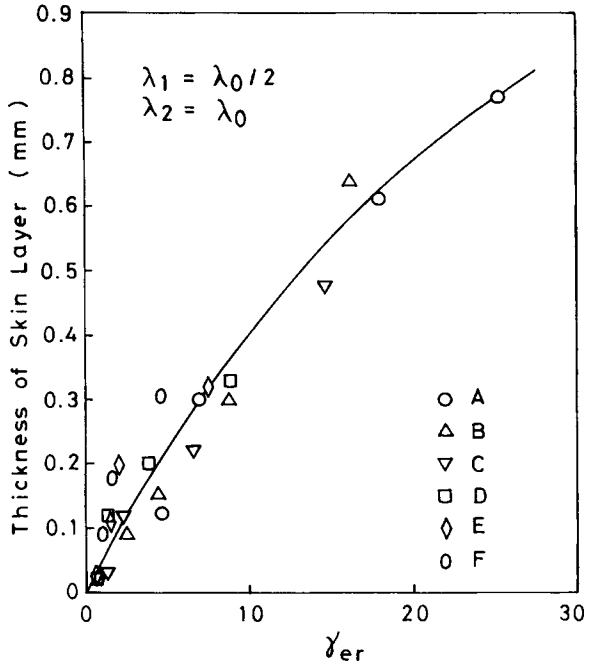

Figure 48 Relation between thickness of skin layer and calculated mean residual recoverable shear strain γ_{er}: $\lambda_1 = \lambda_0/2$, $\lambda_2 = \lambda_0$.

25.1 dg/min under cylinder temperatures of 200–320°C and distributions of higher-order structures in the flow and thickness directions were studied.

Distribution of Higher-Order Structures in Flow Direction

(i) Crystallinity X_c is higher as the MFI of resin and cylinder temperature are higher and scarcely changes in the flow direction.

(ii) The thickness of the skin layer is higher as MFI and cylinder temperature are lower and decreases with going away from the gate.

(iii) a^*-Axis-oriented component fraction $[A^*]$ is higher as MFI and cylinder temperature are higher and increases a little with going away from the gate.

(iv) The crystalline c-axis orientation function f_c is higher as MFI and cylinder temperature are lower and decreases with going away from the gate.

Distribution of Higher-Order Structures in Thickness Direction

(i) X_c is low at the surface region and increases toward the interior. X_c is higher as MFI is higher over all positions across the thickness direction.

(ii) The β-crystals exist at the surface region of about twice the thickness of the skin layer and do not exist at the inner region.

(iii) $[A^*]$ is higher as MFI and cylinder temperature are higher and increases toward the interior.

(iv) f_c is higher as MFI and cylinder temperature are lower. It is the highest at the surface region and decreases toward the interior. There are cases where maximum of f_c which is assumed to be caused by the secondary flow during the cooling and pressure holding process is observed at a midway position in the thickness direction.

Analysis of molecular orientation process

A theoretical analysis of molecular orientation in injection molding was made from a viewpoint of growth of a recoverable shear strain at the gate and its relaxation in the cavity and could considerably well describe the influences of the MFI of resin and cylinder temperature on the mean values and the changes in the flow and thickness directions, of quantities such as the thickness of the skin layer and the crystalline c-axis orientation function f_c which express the degree of molecular orientation.

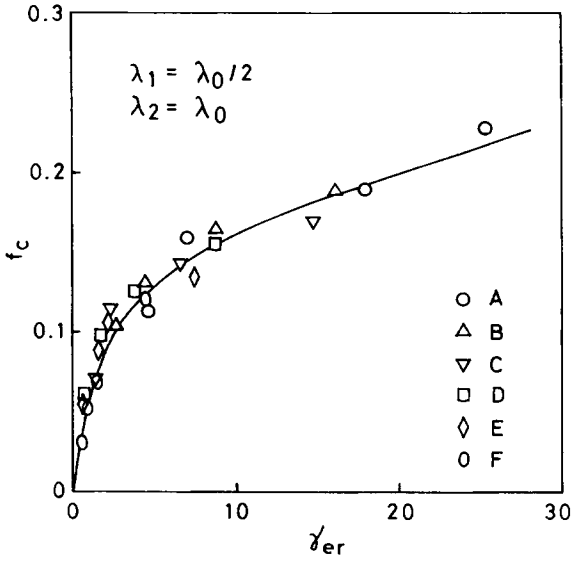

Figure 49 Relation between c-axis orientation function f_c and calculated mean residual recoverable shear strain γ_{er}: $\lambda_1 = \lambda_0/2$, $\lambda_2 = \lambda_0$.

The authors would like to thank Tokuyama Soda Co., Ltd. for permission to publish this paper.

REFERENCES

1. M. R. Kantz, H. D. Newman, Jr., and F. H. Stigale, *J. Appl. Polym. Sci.*, **16,** 1249 (1972).
2. D. R. Fitchmun and Z. Mencik, *J. Polym. Sci. Polym. Phys. Ed.*, **11,** 951 (1973).
3. Z. Mencik and D. R. Fitchmun, *J. Polym. Sci. Polym. Phys. Ed.*, **11,** 973 (1973).
4. G. Menges, G. Wübken, and B. Horn, *Colloid Polym. Sci.*, **254,** 267 (1976).
5. A. Krsova, *Int. Polym. Sci. Technol.*, **4**(10), T/33 (1977).
6. K. Matsumoto, I. Miura, and K. Hayashida, *Kobunshi Ronbunshu,* **36,** 401 (1979).
7. H. Hirose, K. Ito, and T. Kawano, *Plast. Jpn.*, **26**(2), 13 (1980).
8. J. P. Trotignon, J. L. Lebrun, and J. Verdu, *Plast. Rubber Process. Appl.*, **2,** 247 (1982).
9. F. Altendorfer and G. Geymayer, *Plastverarbeiter,* **34,** 511 (1983).
10. F. Altendorfer and E. Seitl, *Plastverarbeiter,* **35,** 144 (1984).
11. F. Altendorfer and E. Seitl, *Kunststoffe,* **76,** 47 (1986).
12. M. R. Kamal, L. Song, and P. Singh, *SPE Tech. Pap. 44th ANTEC,* **32,** 133 (1986).
13. J. P. Trotignon and J. Verdu, *J. Appl. Polym. Sci.,* **34,** 1 (1987).
14. J. P. Trotignon and J. Verdu, *J. Appl. Polym. Sci.,* **34,** 19 (1987).
15. J. Koppelmann, E. Fleischmann, and G. Leiter, *Rheol. Acta,* **26,** 548 (1987).
16. E. Fleischmann and J. Koppelmann, *Kunststoffe,* **77,** 405 (1987).
17. G. Menges, H. Ries, and T. Wiegmann, *Kunststoffe,* **77,** 917 (1987).
18. S. Kubota, *Polym. Prepr. Jpn.*, **36,** 3677 (1987).
19. M. Houska and M. Brummell, *Polym. Eng. Sci.,* **27,** 917 (1987).
20. M. Houska and M. Brummell, *Plaste Kautschuk,* **35,** 83 (1988).
21. M. W. Murphy, K. Thomas, and M. J. Bevis, *Plast. Rubber Process. Appl.*, **9,** 3 (1988).
22. M. W. Murphy, K. Thomas, and M. J. Bevis, *Plast. Rubber Process. Appl.*, **9,** 117 (1988).
23. E. Fleischmann and J. Koppelmann, *Kunststoffe,* **78,** 453 (1988).
24. G. Menges, A. Troost, J. Koske, H. Ries, and H. Stabrey, *Kunststoffe,* **78,** 806 (1988).
25. E. Fleischmann, P. Zipper, and A. Janosi, W. Geymayer, J. Koppelmann, and J. Schurz, *Polym. Eng. Sci.,* **29,** 835 (1989).
26. E. Fleischmann, *Int. Polym. Process.*, **4,** 158 (1989).
27. M. Fujiyama and T. Wakino, *J. Appl. Polym. Sci.*, to appear.
28. M. Fujiyama and S. Kimura, *Kobunshi Ronbunshu,* **32,** 581 (1975).
29. Z. W. Wilchinsky, *J. Appl. Phys.*, **31,** 1969 (1960).
30. W. Weidinger and P. H. Hermans, *Makromol. Chem.*, **50,** 98 (1961).
31. A. Turner-Jones, J. M. Aizilewood, and D. R. Beckert, *Makromol. Chem.*, **75,** 134 (1964).
32. B. Wunderlich, *Macromolecular Physics,* Academic, New York, 1976, Vol. 2.
33. F. H. Moy and M. R. Kamal, *Polym. Eng. Sci.,* **20,** 957 (1980).
34. M. R. Kamal and F. H. Moy, *Polym. Eng. Rev.*, **2,** 381 (1983).
35. M. R. Kamal and F. H. Moy, *J. Appl. Polym. Sci.*, **28,** 1787 (1983).
36. R. L. Ballman and H. L. Toor, *Mod. Plast.*, **38,** 113 (Oct. 1960).
37. J. L. S. Wales, J. Van Leeuwen, and R. Van Der Vijgh, *Polym. Eng. Sci.,* **12,** 358 (1972).
38. G. Menges and G. Wübken, *SPE Tech. Pap. 31st ANTEC,* **19,** 519 (1973).
39. Z. Tadmor, *J. Appl. Polym. Sci.*, **18,** 1753 (1974).
40. E. L. Kalinchev, M. B. Sakovtseva, and E. D. Zhukovskaya, *Int. Polym. Sci. Technol.*, **3**(12), T/29 (1976).
41. H. Janeschitz-Kriegl, *Rheol. Acta,* **16,** 327 (1977).
42. M. Fujiyama and S. Kimura, *J. Appl. Polym. Sci.*, **22,** 1225 (1978).
43. C. D. Han and C. A. Villamizar, *Polym. Eng. Sci.*, **13,** 173 (1978).
44. W. Dietz, J. L. White, and E. S. Clark, *Polym. Eng. Sci.*, **18,** 273 (1978).
45. W. Dietz and J. L. White, *Rheol. Acta,* **17,** 676 (1978).
46. A. I. Isayev and C. A. Hieber, *Rheol. Acta,* **19,** 168 (1980).
47. J. Greener and G. H. Pearson, *J. Rheol.*, **27,** 115 (1983).
48. M. Kohyama, Y. Akane, and T. Okamoto, *Polym. Prepr. Jpn.*, **32**(10), 3089 (1983).
49. P. G. Lafleur and M. R. Kamal, *Polym. Eng. Sci.*, **26,** 92 (1986).
50. M. R. Kamal and P. G. Lafleur, *Polym. Eng. Sci.*, **26,** 103 (1986).
51. M. Fujiyama, *Nihon Reoroji Gakkaishi,* **14,** 152 (1986).
52. M. Fujiyama, Y. Kawasaki, and T. Wakino, *Nihon Reoroji Gakkaishi,* **15,** 191 (1987).
53. M. Fujiyama, Y. Kawasaki, and T. Wakino, *Nihon Reoroji Gakkaishi,* **15,** 203 (1987).
54. H. Mavridis, A. N. Hrymak, and J. Vlachopoulos, *J. Rheol.*, **32,** 639 (1988).
55. J. Greener, R. Kesel, and B. A. Contestable, *AIChE J.*, **35,** 449 (1989).
56. T. Kanai, K. Shimizu, and Y. Uryu, *Int. Polym. Process.*, **4,** 132 (1989).

57. K. Tada, *Fifth Ann. Meeting PPS Prepr.*, 42 (1989).
58. H. S. Carslaw and J. C. Jaeger, *Conduction of Heat in Solid*, 2nd ed., Oxford University Press, Oxford, 1957.
59. H. Heron, S. Pederson, and L. L. Chapoy, *Rheol. Acta*, **15**, 379 (1976).
60. W. Philippoff and F. H. Gaskins, *Trans. Soc. Rheol.*, **2**, 263 (1958).
61. E. B. Bagley, *J. Appl. Phys.*, **28**, 624 (1957).
62. W. W. Graessley, *Adv. Polym. Sci.*, **16**, 1 (1974).
63. W. P. Cox and E. H. Merz, *J. Polym. Sci.*, **28**, 619 (1958).
64. T. Matsumoto, T. Watanabe, and T. Hisamoto, *Kogakuin Univ. Res. Rep.*, **52**, 105 (1982).
65. T. R. Fuller and A. L. Fricke, *J. Appl. Polym. Sci.*, **15**, 1729 (1971).
66. F. G. Danusso, G. Maraglio, W. Ghiglia, L. Motta, and G. Talamini, *Chem. Ind.*, **41**, 74 (1959).
67. D. R. Gee and T. P. Melia, *Makromol. Chem.*, **132**, 195 (1970).
68. E. B. Bagley, *J. Appl. Phys.*, **31**, 1126 (1960).
69. R. B. Staub, *SPE J.*, 429 (April 1960).
70. M. Sakai, H. Fukaya, and M. Nagasawa, *Trans. Soc. Rheol.*, **16**, 635 (1972).

Received December 6, 1989
Accepted November 9, 1990